Anisotropy and variability in polyurethane foams: experiments and modeling

Benjamin Kraus[a], Raj Das[a], Biswajit Banerjee[b,*]

[a] *Dept. of Mechanical Engineering, University of Auckland, New Zealand*
[b] *Industrial Research Limited, 24 Balfour Road, Parnell, Auckland, New Zealand*

Abstract

Modern foam-filled composite products have the advantage of low weight while providing improved shock absorption, acoustic, and thermal properties. Recent investigations of foam-filled thin metal open sections have shown that these composites also have excellent structural properties. However, when optimizing new foam-filled products for structural applications, the material behaviour of each constituent material has to be known before simulations can be performed and potential failure predicted. This paper presents the results of mechanical characterization tests of a low density polyurethane (PU) foam and describes a new anisotropic plasticity model that can be used for large deformation simulations of foams and foam-filled composites. Uniaxial tension and compression, triaxial compression, simple shear, and fracture toughness tests on the PU foam are described. These tests indicate that the foam is strongly anisotropic, exhibits a significant amount of variation between samples, and that a non-associated flow rule is needed for predictive simulations. The new piriform (pear-shaped) anisotropic yield surface is convex, has excellent smoothness properties, is able to predict the observed behavior of the foam, and reduces to an ellipsoidal form for some choices of parameters. The yield function has the potential to be applied to a large variety of foams as well as soils, rocks, bone, and concrete.

Keywords: polyurethane foam, uniaxial tension, uniaxial compression, triaxial compression, simple shear, fracture toughness, anisotropy, variability, anisotropic yield surface, non-associated plasticity, hardening models

---

Contents

---

[*] Corresponding author.

Email addresses: `benjamin.kraus@engineering-kraus.com` (Benjamin Kraus), `r.das@auckland.ac.nz` (Raj Das), `b.banerjee.nz@gmail.com` (Biswajit Banerjee)

Preprint submitted to Elsevier *January 24, 2013*

1. Introduction

Industrial polymeric foams can be classified into two broad categories based on the amount of material property variability observed in the manufactured product. In the first category are low variability foams such as those used in sandwich composites for boats and aircraft. These foams are usually manufactured in bulk and their properties are relatively tightly controlled. In the second category are highly variable foams that are produced in small batches. Examples include foam-filled metal sections used in construction. Both categories of foam are anisotropic because the manufacturing process causes preferential evolution of the foam in the "rise" direction during the foaming process.

The typical design procedure for novel foam-filled structures involves a cost-based selection of metal sections and foaming agents, foam manufacture and filling of the sections, and post-cure testing of the sections (typically bending and buckling tests). This procedure limits the length of the sections that can be tested and the number of designs that can be evaluated. For foam-filled structures, quality control is typically perfunctory though some attention is paid to foam density and the control of large voids.

Consider low density polyurethane (PU) foams used in filled metal sections. Predictive simulations remain underutilized for such applications primarily because such foams are rarely well-characterized and therefore numerical models provide only qualitative results. Extensive research has been conducted into the mechanical properties of polymeric foams, yet complex foam behaviour beyond isotropic linear elasticity is rarely considered in the design process. Clearly, a more advanced design approach is needed that considers the complexity of foam behaviour particularly when foam composite products with high strength, durability, and life are sought.

The literature on PU foams indicates that while structure-property relations can provide qualitative estimates for the behavior of foam of a particular density, quantitative descriptions require extensive material testing of the particular foam under consideration. This is mainly because of the variability of foam properties and structure and the absence of systematic characterisation of various types of foams. An additional challenge is that existing material models for polymeric foams are inadequate for modeling anisotropic foams, particularly for large deformations.

This paper seeks to address some of the challenges faced in the design of PU foam-filled structures by making the following primary contributions:

1. a detailed characterization of the anisotropic elastic, plastic, and failure behavior of a low density (45 kg/m^3) PU foam and identification of confidence bounds on the variability of the foam, and
2. the development of a new anisotropic, smooth, bounded, piriform (pear-shaped) yield surface (19) from which many existing models for foams and geomaterials can be derived as special cases.

The organization of the paper is as follows. Section 2 explains the motivation for this study and provides background on characteristics that are of interest in foam-filled composites for construction. Section 3 deals with experimental characterization of a typical low density PU foam used in construction and Section 4 explores phenomenological models that can be used to predict the macroscopic response of the foam. The principal observations of the paper are reiterated in Section 5.

2. Background

2.1. Motivation: foam-filled sections

There is an extensive literature on the characterization and modeling of the *crush behavior* of foam filled *closed-sections*, for example, Reddy and Wall (1988); Niknejad et al. (2012) (PU foam/circular section), Reid et al. (1986); Santosa et al. (2000) (metal foam/box section). Most of these composite structures were designed with energy absorption in mind. Examples of studies on the *bending behavior* of foam-filled sections include studies on filled-beams (Santosa and Wierzbicki, 1999; Shahbeyk et al., 2004) and car-bumper simulant structures, e.g., Zarei and Kröger (2008). *Open-sections*, such as those used in the construction industry, have been studied less frequently but examples can be found in the literature, e.g, Song et al. (2005). These and numerous other studies indicate that foam fillers (whether metal or polymer) can provide significant benefits. Most numerical studies of foam-filled structures assume the validity of isotropic ellipsoidal plastic yield models such as those developed by Deshpande and Fleck (2000). The current focus in the field is on optimization of designs (Zarei and Kröger, 2008) and on the failure of the interface between foam and metal (Kraus, 2012).

Our study was motivated by the preliminary work by Exley et al. (2010a,b, 2011a,b) who demonstrated the superiority of open-section steel-foam composite beams (especially under bending and torsion). It was felt that further improvements could be achieved by adjusting the design according to specific load cases that are expected during the service life of these composite beams. However, developing an optimum structural design requires an in-depth understanding of the mechanical behaviour of the constituent materials. These include the characterization of the foam and the foam-metal interface and the development of adequate material models that can be used for numerical simulations during the design process.

The existing literature has been found to be deficient both in material characterization of low density PU foams and material models that can describe the mechanical behavior of these foams over a large range of deformations. This paper attempts to close that gap by describing the detailed characterisation of a low density PU foam. The material parameters in three orthogonal directions of the PU foam are measured using uniaxial tension, uniaxial and triaxial compression, simple shear tests, and three-point bend fracture toughness tests on foam specimens. Foam-metal interfacial cohesion and adhesion properties were also measured and details can be found in Kraus (2012). Because existing material models were found to be inadequate, the measured data were used to develop an empirical anisotropic elastic-plastic model that is valid for a large range of loading conditions. The model includes a novel piriform yield surface, potential non-associated flow rules, and related anisotropy evolution and hardening models. Existing structure-property relations for foams could potentially be used to extend the model for application to a larger range of foam types.

2.2. Foam structure-property relations

One of the defining characteristics of a foam is its mass density (Gibson and Ashby, 1999). The mechanical, acoustic, electrical and thermal properties of a foam material are strongly dependent on its density. Numerous studies of sandwich panels with foam cores have shown that the structural strength of a panel increases if a higher density foam core is used (Sharaf et al., 2010; Daniel and Gdoutos, 2010). It is also well known that yield strength and elastic modulus increase as the density of the foam increases (Gibson and Ashby, 1999; Kabir et al., 2006).

The PU foam under consideration in this paper is closed-cell. For isotropic closed-cell foams, if we ignore the gas pressure inside the cells, the elastic moduli can be expressed as quadratic functions of the relative density ($\rho_{\text{foam}}/\rho_{\text{solid}}$) of the foam.[1] The subscript foam indicates an effective property of the foam while the subscript solid indicates the corresponding property of solid polyurethane. For the low density foams considered in this paper, the ratio $\rho_{\text{foam}}/\rho_{\text{solid}}$ is approximately 0.04 and the linear term in the quadratic function is dominant (Gibson, 2000), i.e.,

$$\frac{E_{\text{foam}}}{E_{\text{solid}}} \approx \alpha_{12} \frac{\rho_{\text{foam}}}{\rho_{\text{solid}}} \quad \text{and} \quad \frac{G_{\text{foam}}}{E_{\text{solid}}} \approx \alpha_{22} \frac{\rho_{\text{foam}}}{\rho_{\text{solid}}} \tag{1}$$

---

[1] Micromechanical considerations and experimental data point to expressions of the form (Gibson and Ashby, 1999)

$$\frac{E_{\text{foam}}}{E_{\text{solid}}} \approx \alpha_{11} \left(\frac{\rho_{\text{foam}}}{\rho_{\text{solid}}}\right)^2 + \alpha_{12} \frac{\rho_{\text{foam}}}{\rho_{\text{solid}}} \quad \text{and} \quad \frac{G_{\text{foam}}}{E_{\text{solid}}} \approx \alpha_{21} \left(\frac{\rho_{\text{foam}}}{\rho_{\text{solid}}}\right)^2 + \alpha_{22} \frac{\rho_{\text{foam}}}{\rho_{\text{solid}}}$$

where E is the Young's modulus, G is the shear modulus, ρ is the mass density, and α_{12}, α_{22} are constants that depend on the bulk material.

The value of E_{solid} can vary significantly with the manufacturing process and cell shape. The estimation of the effective Young's modulus of a given foam from average properties of solid PU is therefore difficult. The mass density of solid polyurethane can also vary, but the range of variation is small when compared with the effective mass density of a typical foam. In contrast, the effective Poisson's ratio of PU foams at small deformations is usually around 0.3 with a relatively small amount of variation. The effective Poisson's ratio for typical PU foams tends to zero at moderate compressive strains and to 0.5 at moderate tensile strains (Choi and Lakes, 1992).

A large number of foams have anisotropic material properties. A number of authors, e.g., Huber and Gibson (1988); Gibson and Ashby (1999); Subramanian and Sankar (2012), have conducted detailed studies on the effect of structural anisotropy on material properties. For example, Huber and Gibson (1988) showed that the anisotropy of the cell structure in PU foam affects the modulus and collapse stress of the cells significantly more than the fracture toughness of the foam. From a micromechanical point of view, Gibson and Ashby (1999) concluded that the shape anisotropy ratio[2] of a cuboid foam cell model with square cross-section is directly related to the YoungâĂŹs moduli, shear moduli, stresses at plastic cell collapse, and the fracture toughness in different directions. More complex models involving tetradecahedral have also been used to better predict structure property relations for foams, for example Zhu et al. (1997); Roberts and Garboczi (2002); Subramanian and Sankar (2012). However, the focus has mainly been on open cell structures and elastic properties.

The deformation behavior of foams under uniaxial tensile and compressive loads can be used to classify foams into three groups: elastomeric, elastic-plastic, and elastic-brittle (Gibson and Ashby, 1999). The PU foam under consideration is elastic-brittle in uniaxial tension but elastic-plastic in compression and pure shear. In tension fracture occurs abruptly whereas in compression failure is accompanied by plastic yield caused by the sequential crushing of foam cells.

Experimental data suggest that the stress at initial yield in compression depends linearly on the relative density of a foam (Gibson and Ashby, 1999). Models in the literature simplify the plastic deformation process by assuming a perfectly plastic phase during which the dominant deformation mode is buckling followed by a linear hardening stage (Gibson et al., 1989; Schreyer et al., 1994). Most foam plasticity models have been empirically derived. However, micromechanical models (particularly for open foams) indicate yield surfaces that are ellipsoidal in shape (see, for example, Deshpande and Fleck (2000); Zhang and Lee (2003)). The plastic Poisson's ratio in compression of many foams (both open and closed-cell) is close to zero requiring the choice of a reduced ellipsoidal yield potential and non-associativity (Schreyer et al., 1994; Deshpande and Fleck, 2001) of the flow rule. The effect of foam structure on the form of the flow rule remains poorly understood though some studies of truss structures (such as those used in open-cell foams) suggest that associated flow rules can be derived from micromechanical considerations (Mohr, 2005).

The fracture behaviour of a rigid polyurethane (PU) foam of a density range between 32 and 360 kg/m^3 was investigated by McIntyre and Anderton (1979) through testing of single edge notch specimens. Their investigations showed that the fracture toughness (K_{Ic}) increased with the foam density. The data exhibited a power law relation with an exponent of 1.17 and a nearly linear relation at low densities. No such linear relation was observed between the measured critical strain energy release rate G_{Ic} and the foam density. An alternative approach has been to use double cantilever beam specimens (e.g., Fowlkes (1974)). However, the technique is unattractive for low density foams because of difficulties encountered in specimen preparation and loading.

The fracture toughness of polyvinyl chloride and PU foams was also measured by Kabir et al. (2006) using single edge notch specimens. But their measurements of PU foam showed higher values for K_{Ic} than observed by McIntyre and Anderton (1979). For a PU foam with a density of 240 kg/m^3 they found the fracture toughness to be 0.30 ± 0.02 MPa m$^{1/2}$ which is about two times higher than that for PU foam at the same density (McIntyre and Anderton, 1979). The fracture toughness of PU foam was also determined by Jin et al. (2007b). In this study the test method used single edge notch specimens of density ~ 320 kg/m^3 and determined K_{Ic} based on linear elastic fracture mechanics. The fracture toughness for this foam density was found to be 0.215 MPa m$^{1/2}$ which coincides with the

---

[2] The shape anisotropy ratio in the Gibson-Ashby model is defined as $R = h/l$ where h is the height of a rectangular shaped foam cell and l the length of its squared cross section

results from McIntyre and Anderton (1979). The fracture toughness values determined by Huber and Gibson (1988) from tests on PU foams with densities ranging between 32–160 kg/m^3 are higher than those determined by McIntyre and Anderton (1979) and Jin et al. (2007a), but lower than those determined by Kabir et al. (2006). The variation in fracture toughness indicated by the above results show that even nominally identical foams can have a large amount of variability in the energy needed for fracture to occur.

Multiple studies on foams show a strong strain rate dependency of the material (Sarva et al., 2007; Roland et al., 2007). The strain rate hardening effect has been found to be more pronounced for foams with high density (Bouix et al., 2009). These studies indicate that the test procedures and approaches to characterise PU foams need to be conducted within a tightly controlled strain rate regime. A direct comparison of measured material properties, such as ultimate strength or yield stress, from different material tests would not be valid if the results were obtained through tests at different strain rates. Though strain rate effects are clearly important, particularly for shock absorption applications, in this paper we do not explore the rate-dependent behavior of the low density PU foam.

Clearly, the density of the foam is not sufficient for characterization and more information of the foam microstructure is needed. The effect of manufacturing process on the foam microstructure and the properties of the matrix material is important but has received limited attention in the literature (Everitt et al., 2006; Yue et al., 2007). The test procedure, strain rates, and environmental conditions also contribute to the variability in the test data reported in the literature. These observations demonstrate the problems with using data obtained from the literature. Whenever the precise material behaviour of specific foam is required, a series of tests have to be conducted on the particular material under consideration. If the results are found to coincide with those from other sources, further properties can be used from the literature instead of more extensive testing.

Even for well manufactured foams, the mechanical properties are influenced strongly by the microstructure because the foam geometry evolves with deformation. This leads to difficulties when a complete description of a particular polymeric foam is sought for design and failure prediction. Few studies exist that closely examine a single material property on exactly the same foam material at the identical density. Thus a full characterisation of one polymeric foam cannot necessarily be obtained from the literature even though a substantial number of studies on different properties of the material might be available.

Ideally, given the detailed understanding of a particular PU foam its microstructure it should be possible to determine the mechanical behavior of any other PU foam using structure-property relationships. For example, a tensor shape analysis such as that suggested by Schröder-Turk et al. (2011) can then be used to relate the microstructure and properties of a new foam to the well calibrated foam. Some progress has been made in this regard (see, for example, Rodríguez-Pérez et al. (2005); Burteau et al. (2012)) but structure-property relations significantly superior to those discussed in Gibson and Ashby (1999) are yet to be developed, particularly for closed-cell foams. The work presented in this paper represents the characterization phase of such a research programme. Structure-property relationships will be explored in future work.

3. Experimental characterization

Many investigations have been conducted to measure the mechanical properties of polymer materials and polymer foams (McIntyre and Anderton, 1979; Huber and Gibson, 1988; Kabir et al., 2006; Jin et al., 2007a,b; Sharaf et al., 2010). Most studies, however, only focus on tests to determine one or two properties of a material, rather than conducting a full field study that describes all relevant mechanical properties of a specific foam. In this work we present experimental data on uniaxial tension, uniaxial compression, triaxial compression, simple shear, and fracture toughness tests on a low density PU foam. While some of the details of experimental characterization of the PU foam are described in this section of the paper, the description is brief and significantly more detail can be found in Kraus (2012).

3.1. Manufacture and microstructure

The PU foam was manufactured through a chemical reaction of the liquid isocyanate and polyol. This manufacturing process is common in the construction industry. The reactants were mixed in a ratio of 1.1 to 1 by weight and cast into a mould where they reacted, expanded, and cured for 24 hours until the resultant foam reached its full mechanical and chemical stability. The mould that was used to manufacture the foam panels had dimensions of

600 mm × 90 mm × 250 mm. Three material directions can be defined on the basis the orientation of the mould with respect to gravity as shown in Figure 1. Direction 1 represents the direction in which the foam expands the most during reaction and expansion (called the foam rise direction). The foam cells were elongated along direction 1 compared to the two transverse directions.

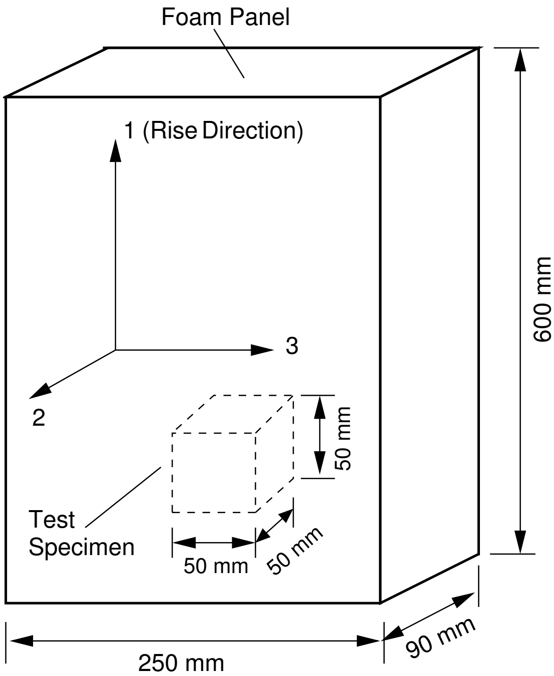

Figure 1: Definition of material directions and foam orientation used in the characterization of PU foams. Panel and typical specimen dimensions are also shown.

Magnified photographs of the foam microstructure taken through a light microscope at 40× magnification are shown in Figure 2. The PU foam is clearly closed-cell. There appears to be a distinct elongation of the cells in the rise direction when viewed from direction 3 (1–2 plane) but no obvious elongation can be seen when the cells are viewed from direction 2 (1–3 plane). The image taken from direction 1 (2–3 plane) shows cells that appear isotropic.

3.2. Poisson effect

Computational algorithms that are used to simulate the large strain behavior of foams require a constitutive relationship between the Cauchy (true) stress and a large strain measure such as the Hencky (logarithmic or true) strain. Typical numerical simulations of foams assume that engineering and true stress-strain curves are identical and therefore interchangeable. Choi and Lakes (1992) showed that conventional foams have Poisson's ratios close to 0.3 for small strains, but as the strain increases these values approach 0 in compression and 0.5 in tension. The true stress in a foam is therefore a nonlinear function of the engineering strain and the Cauchy stress and the engineering stress can be different at moderate strains.

Representative values of the Poisson's ratio as a function of engineering strain and sigmoidal fits to the data are shown in Figure 3. The sigmoidal curve fits to the experimental data have the form

$$\nu(\varepsilon) = \begin{cases} \nu_{0t} + \dfrac{0.5 - \nu_{0t}}{1 + \exp[\alpha_\nu(\varepsilon + \varepsilon_{0t})]} & \text{for} \quad \varepsilon < 0 \\ \dfrac{\nu_{0c}}{1 + \exp[\beta_\nu(\varepsilon - \varepsilon_{0c})]} & \text{for} \quad \varepsilon \geq 0 \ \text{compression} \end{cases} \tag{2}$$

where $\nu_{0t} = 0.2987$, $\nu_{0c} = 0.3060$, $\alpha_\nu = 20$, $\beta_\nu = 14$, $\varepsilon_{0t} = 0.25$, $\varepsilon_{0c} = 0.28$. The two curves coincide at $\varepsilon = 0$ with $\nu = 0.3$.

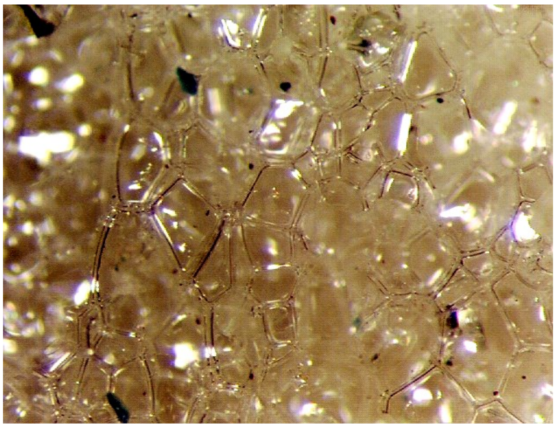

(a) 1–3 plane.

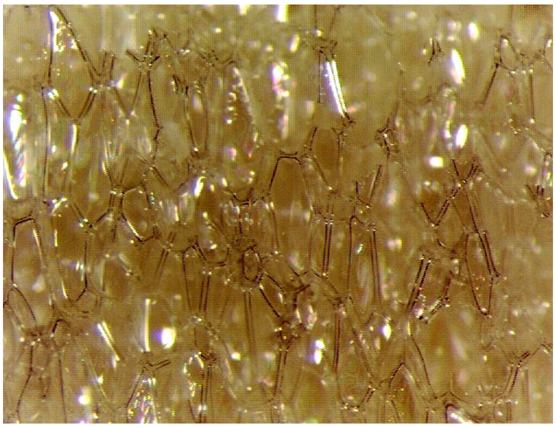

(b) 1–2 plane.

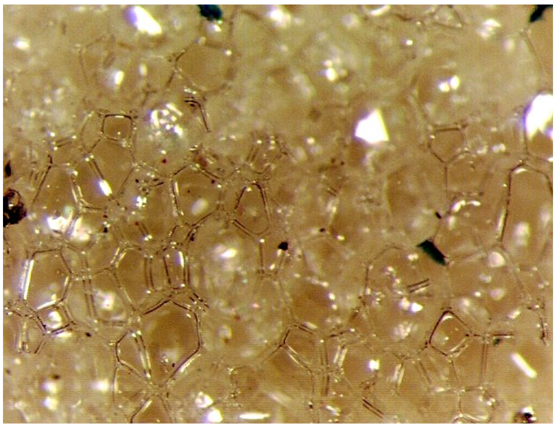

(c) 2–3 plane.

Figure 2: Cross-sections of the foam as seen under a light microscope.

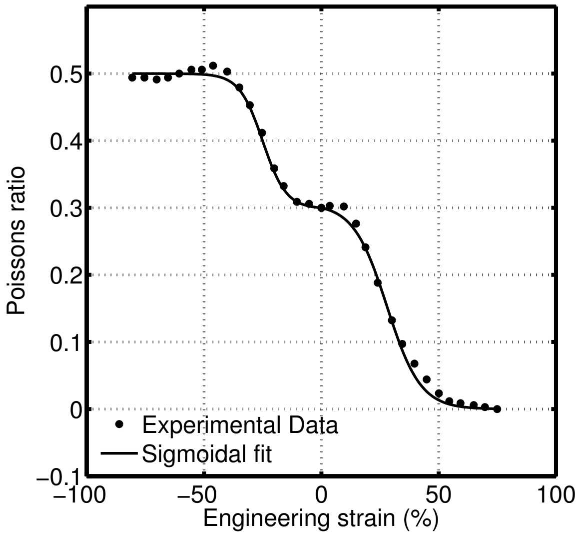

Figure 3: Possion's ratio as a function of engineering strain (compression positive) for a conventional polyurethane foam. The experimental data points have been obtained from Choi and Lakes (1992).

With the convention that compressive strains are positive, the true stresses and logarithmic (true) strains in uniaxial tests can be computed using

$$\sigma_{\text{true}} = \frac{\sigma}{[1+\nu(\varepsilon)\varepsilon]^2} \quad \text{and} \quad \varepsilon_{\text{true}} = \ln(1-\varepsilon) \tag{3}$$

where σ_{true} is the true stress, $\varepsilon_{\text{true}}$ is the true strain, σ is the engineering stress, and ε is the engineering strain. The true stress-true strain curves for the uniaxial tests discussed in this paper have been computed with the expressions in equations (3) and (2). Since the density of the foam samples is never exactly 45 kg/m^3, the stress-strain curves have been scaled using equations (1) so as to correspond to that density. Note that while the proposed Poisson effect model depicted in Figure 3 fits our experimental observations qualitatively, the actual values for a particular PU foam may vary with microstructure.

3.3. Uniaxial tension tests

Tension tests were performed on foam cubes of 50 mm × 50 mm × 50 mm, that were machined out of cast foam panels. The test setup followed the standard ASTM-C297-04 (2010). The YoungâĂŹs modulus in tension E_t and the maximum strain $\varepsilon_t^{\max}$ were calculated following ASTM-D3039-08 (2008) and ASTM-D638-10 (2010). The setup according to ASTM-C297-04 (2010) was chosen because it is designed for thick sandwich materials, whereas the standards ASTM-D3039-08 (2008) and ASTM-D638-10 (2010) use a dog bone sample which is unsuitable to manufacture out of the foam. The tensile deformation rate was 2 mm per minute (strain rate of ∼0.0006 per minute). Six samples from two separately manufactured foam panels were tested in directions 1 and 2, and four samples from one panel were tested in direction 3.

The true stress-true strain curves in tension for the three directions (1, 2 and 3) are shown in Figure 4. The foam is brittle in tension. There is a significant amount of variability between samples even after the data have been corrected for variations in mass density. The foam is stiffer in direction 1 (rise direction) compared to directions 2 and 3. The smaller amount of variation in direction 3 indicates that a large portion of the variability arises from the panel manufacturing process.

Table 1 lists the average values of density ρ, ultimate tensile strength σ_t, tensile strain at failure ε_t, and the tensile YoungâĂŹs modulus E_t. Direction 1 shows the highest variation for E_t and σ_t but comparatively little variability in the strain at failure. The anisotropy of the foam can be explained by its cellular structure. In the

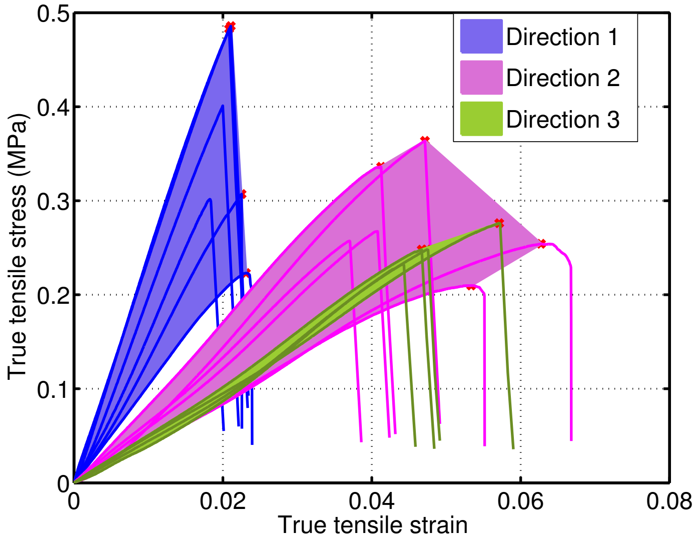

Figure 4: Uniaxial tension stress-strain data for PU foam in three loading directions.

Table 1: Tensile properties of closed cell polyurethane foam. The percent value inside the round brackets indicates the coefficient of variation.

	ρ (kg/m^3)	E_t (MPa)	σ_t (MPa)	ε_t
Direction 1	44.7 ± 1.58	19.0 (±28.5%)	0.37 (±29.1%)	0.02 (±8.3%)
Direction 2	43.9 ± 1.15	6.1 (±28.5%)	0.28 (±20.3%)	0.05 (±20.4%)
Direction 3	44.0 ± 1.53	4.6 (±6.5%)	0.25 (±7.2%)	0.05 (±11.6%)

Table 2: Ratios of average tensile properties in different directions.

Ratio	E_t	σ_t	ε_t
1–2	3.1	1.3	0.4
1–3	4.1	1.5	0.4
2–3	1.3	1.1	1.0

foam rise direction the cells are elongated and relatively well aligned leading to a stiffer response. The measured low strain at break appears to reflect the strain at break of the bulk PU material. There is little variance between samples because the homogeneous PU material has a relatively consistent stress and strain at failure compared to the foamed material.

The ratios of the tensile mechanical properties of the PU foam in different directions are shown in Table 2. The foam is significantly stiffer and exhibits a higher strength at failure in direction 1 (the foam rise direction) and is approximately isotropic in the 2–3 plane. The strain at failure for tension in direction 1 is around half that in the other two directions. The tensile strength is 1.3 and 1.5 times higher than in directions 2 and 3. The elongated cells in the rise direction cause the higher observed strength in direction 1 and also make the foam less stiff along the two transverse directions (directions 2 and 3). The relatively isotropic response in the transverse directions also indicates that the cell structure is elongated along the foam rise direction but has an isotropic shape in the 2–3 plane. This is reasonable from the manufacturing perspective as there was very little expansion of the foam in directions 2 and 3 during curing.

3.4. Uniaxial compression tests

Fifteen 50 mm foam cubes were machined from a single panel and tested in uniaxial compression, five each in the three main material directions. The test procedure followed standards ASTM-D1621-10 (2010) and ISO-844 (2001). The test fixture was chosen according to ISO-844 (2001) where two fixed parallel plates are used to compress a specimen. The compression rate was 5 mm per minute (strain rate ∼ 0.0016 per second).

Figure 5 shows the compressive true stress-true strain curves for the samples in the three directions (1, 2 and 3). The figure shows that the stress-strain behavior is very different in the three orthogonal directions and the PU foam is highly anisotropic in compression. However, the properties in the plane transverse to the rise direction are similar except for the initial hardening modulus in direction 2. An examination of the slopes of the stress-strain curves indicates that a rapid increase in hardness begins at a true strain of ∼1.0 (engineering strain ∼60%) in all three directions. The theoretical maximum densification is reached at a true strain of ∼3.2 (engineering strain ∼96%) at which stage there are no voids left and the foam density equals the density of pure PU (∼1185 kg/m^3).

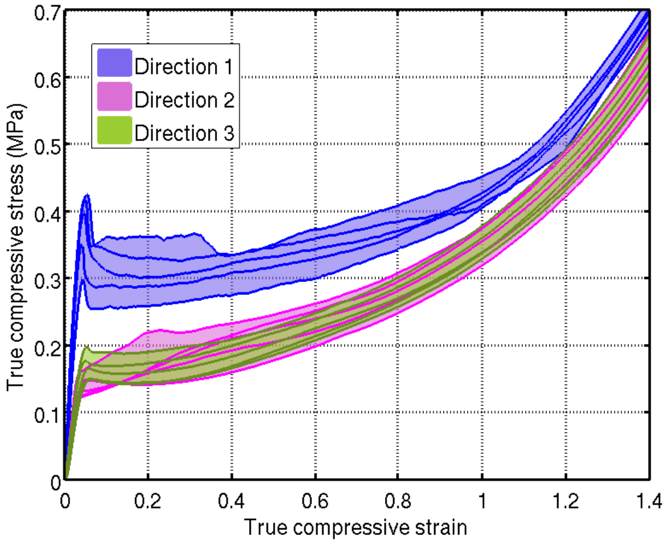

Figure 5: Uniaxial compression stress-strain data for PU foam in three loading directions.

The average mechanical properties in uniaxial compression and the coefficient of variation are listed in Table 3. Ratios of the average properties in the three directions are given in Table 4. The compressive Young's modulus (E_c) in the rise direction is approximately 3 times that in directions 2 and 3. However, there is around 35% of variation in the modulus in direction 3 and around 20% in direction 2. The true strain at initial yield (ε_{yc}) is ∼30% lower in the rise direction than in the transverse directions. In contrast, the true stress at initial yield (σ_{yc}) in the rise direction is approximately twice that in the other two principal material directions.

The average initial hardening modulus[3]($H_{\varepsilon_p=0}$) is close to zero in directions 1 and 3. However, the initial hardening modulus in direction 2 is around 10 times that in the other two directions. As the strain approaches the full densification state, the hardening moduli ($H_{\varepsilon_p=1.4}$) in the three directions become nearly identical.

To further investigate the anomalous initial hardening behavior in the 2–3 plane (see Table 4), a second set of foam cubes was manufactured from a different foam panel. Nine 50 mm cubes were machined from of the foam slab of which four were oriented such that the loading axis was at an angle of 30° with respect to direction 2 while the remaining five were at 60° to direction 2. The cubes were loaded in compression along the loading axis. The

---

[3] The hardening modulus (H) at a given strain is defined as the tangent to the stress-strain curve at that strain. The initial hardening modulus is the value of H at zero equivalent plastic strain (ε_p). The apparently large amount of variation in these values of the initial hardening modulus in Table 3 is due to their small magnitudes.

Table 3: Average uniaxial compressive properties of the polyurethane foam in directions 1, 2 and 3. The strains in the table are true (logarithmic) strains. The coefficients of variation are shown as percentages inside round brackets.

	ρ (kg/m^3)	E_c (MPa)	σ_{yc} (MPa)	ε_{yc}	$H_{\varepsilon_p=0}$ (MPa)	$H_{\varepsilon_p=1.4}$ (MPa)
Direction 1	43.41 ± 1.67	12.44 (± 13.47 %)	0.31 (± 13.50 %)	0.029 (± 9.71 %)	0.022 (± 87.28 %)	1.18 (± 1.49 %)
Direction 2	43.48 ± 0.78	4.61 (± 19.57 %)	0.14 (± 14.20 %)	0.039 (± 17.01 %)	0.22 (± 55.22 %)	1.48 (± 11.82 %)
Direction 3	43.98 ± 0.90	3.96 (± 34.74 %)	0.16 (± 11.07 %)	0.046 (± 9.57 %)	0.021 (± 83.78 %)	1.48 (± 9.61 %)

Table 4: Ratios of average compressive properties of the polyurethane foam.

Ratio	E_c	σ_{yc}	ε_{yc}	$H_{\varepsilon_p=0}$	$H_{\varepsilon_p=1.4}$
1–2	2.7	2.3	0.7	0.1	0.8
1–3	3.1	1.9	0.6	1.1	0.8
2–3	1.2	0.8	0.9	10.5	1.0

samples at an angle of 30° to direction 2 had on average $E_c = 3.8$ MPa, $\sigma_{yc} = 0.13$ MPa, $\varepsilon_{yc} = 0.08$, and $H_{\varepsilon_p=0} = 0.126$ MPa. The samples at an angle of 60° to direction 2 showed average values of $E_c = 5.9$ MPa, $\sigma_{yc} = 0.18$ MPa, $\varepsilon_{yc} = 0.04$, and $H_{\varepsilon_p=0} = 0.04$ MPa. These results show that the absence of a sharp transition from elastic to plastic behavior in direction 2, unlike that observed in directions 1 and 3, is also seen in samples oriented at 30° to direction 2 but not in samples oriented at 60° to that direction.

Cyclic loading-unloading tests on six PU foam samples extracted from a different panel exhibited the behavior shown in Figure 6. The behavior of the sample loaded in direction 2 in the figure confirms that the initial hardening effect in direction 2 is plastic and not nonlinear elastic. Similar behavior has been observed by Xu et al. (2011) and is probably caused by thicker cell walls in the 1–3 plane that inhibit buckling. Further investigation of the effect is needed. The secant modulus in loading and unloading decreases slightly as the plastic strain increases (for small strains). However, the change in elastic modulus with strain is smaller for a single sample than between samples.

3.5. *Triaxial compression tests*

Several triaxial compression tests were performed with a pressure cell in order to observe the PU foam behaviour under multi-axial loading. The testing methods were based on the standards ASTM-D4767-11 (2011) and ASTM-D2850-03a (2007) as well as on the established work by Bishop and Henkel (1962) and Head (1980).

Cylindrical specimens of diameter 38 mm and length 76 mm were machined from one foam panel. Five samples were made with the axis of the samples oriented along direction 1 and five along direction 3. The samples were pressurized to different pressures and then loaded axially to failure. Four of the samples axially loaded in direction 1 were pressurized to mean pressures of 72, 93, 116, and 143 kPa. The fifth sample was loaded hydrostatically. For the samples axially loaded in direction 3, the average applied pressures over the duration of the tests were 29, 45, 65, 89, and 115 kPa. A uniform axial compression rate of 0.025 mm per second (axial strain rate of ∼0.0003 per second) was used during each test. Unlike in the uniaxial tests, the cross-sectional areas of the specimens decreased noticeably during the triaxial tests due to the applied pressure.

Figure 7 shows plots of the deviatoric true stress versus the true axial strain from the triaxial tests[4] The samples loaded axially in the rise direction (direction 1) of the foam yield at higher deviatoric stresses than the samples loaded in the transverse direction (direction 3). One of the samples loaded axially in direction 1 shows strong

---

[4] The experimental data were noisy at the higher confining pressures, particularly for the samples that were axially loaded in direction 1. Noise has been reduced in the plotted data with the help of a Gaussian filter. Note that the sample tested at a confining pressure of 143 kPa appeared to have yielded before a significant axial load could be applied.

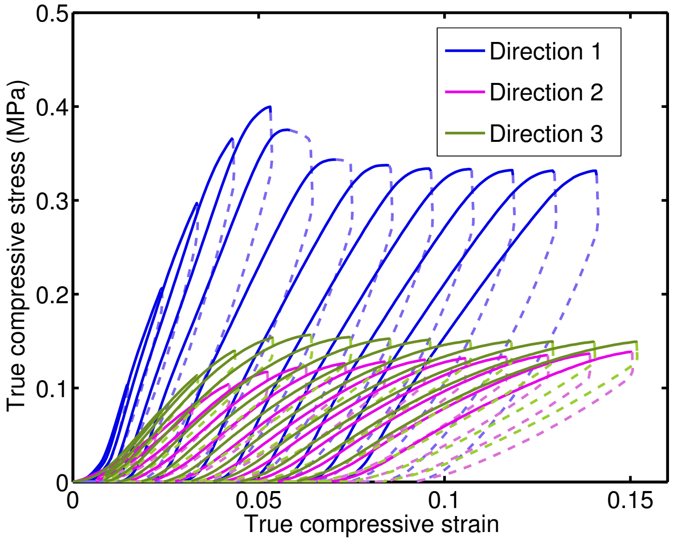

Figure 6: Typical uniaxial compression stress-strain plots for PU foam in three loading directions under cyclic loading (solid line) and unloading (dashed line).

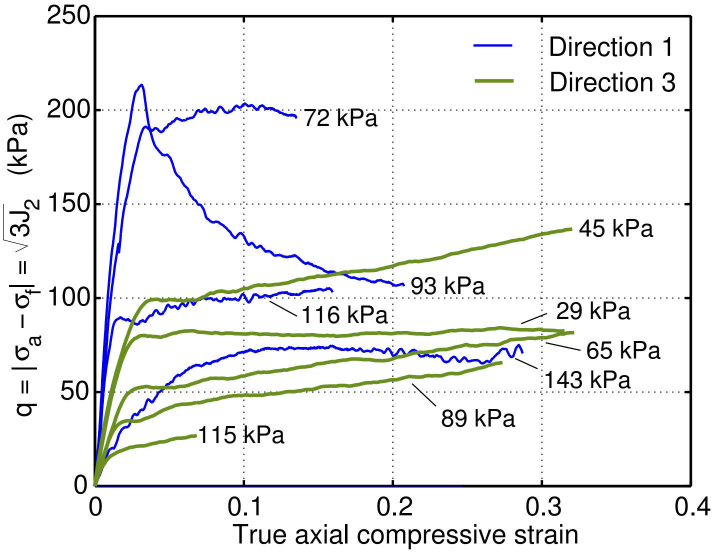

Figure 7: Deviatoric true stress as a function of the axial compressive strain for PU foam. J_2 is the second principal invariant of the deviatoric stress. The numbers in MPa next to the plots indicate the applied fluid pressure.

softening after the peak deviatoric stress is reached while the rest indicate a small amount of hardening. On the other hand, the samples axially compressed in direction 3 exhibit almost linear hardening up to a compressive strain of 0.2 except for one sample that is almost perfectly plastic. If we compare these plots to those shown in Figure 5, we observe that the PU foam fails earlier under triaxial states of stress indicating that these tests are exploring a "cap" like region of the yield surface.

Plots of the pressure (mean stress) as a function of the logarithmic volumetric strain are shown in Figure 8. Most of the samples show negative incremental bulk moduli immediately after yield. This behavior is similar to that observed by Moore et al. (2006) (in hydrostatic tests) indicating buckling of cell walls. The hydrostatic test shows an increase in mean stress followed by a plateau as the volumetric strain increases.

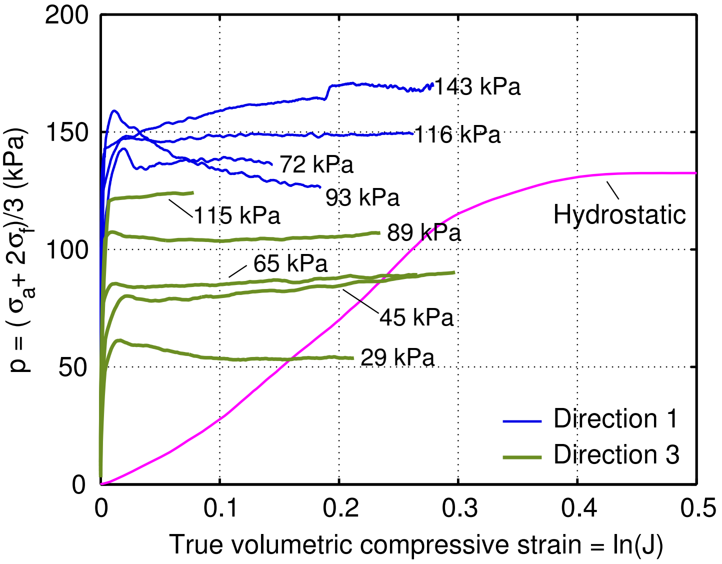

Figure 8: Pressure (mean stress) as a function of the logarithmic volumetric strain for PU foam. σ_a is the axial true stress, σ_f is the fluid pressure in the triaxial cell, and $J = \rho_0/\rho = V/V_0$ is the determinant of the deformation gradient.

Equivalent strains. The deformation of the foam during uniaxial and triaxial compression tests includes not only a volumetric component but also a distortional component. Calibration of the hardening behavior of the foam is therefore easier if a scalar equivalent strain, containing volumetric and deviatoric strain contributions, is used to characterize the deformation. For consistency with the plasticity models discussed later, we define the equivalent strain corresponding to a given strain tensor $\boldsymbol{\varepsilon}$ as

$$\varepsilon_{\text{eq}} := \|\boldsymbol{\varepsilon}\| = \sqrt{\boldsymbol{\varepsilon} : \boldsymbol{\varepsilon}}\,. \tag{4}$$

For the uniaxial and triaxial experiments discussed in this paper, the deformation gradient ($\boldsymbol{F}$), the corresponding right stretch tensor ($\boldsymbol{U}$), and the Hencky strain ($\boldsymbol{\varepsilon}$) can be expressed in reference material coordinates as

$$\boldsymbol{F} = \boldsymbol{U} \equiv \begin{bmatrix} \lambda_a & 0 & 0 \\ 0 & \lambda_t & 0 \\ 0 & 0 & \lambda_t \end{bmatrix} \quad \text{and} \quad \boldsymbol{\varepsilon} \equiv \begin{bmatrix} \ln(\lambda_a) & 0 & 0 \\ 0 & \ln(\lambda_t) & 0 \\ 0 & 0 & \ln(\lambda_t) \end{bmatrix} \tag{5}$$

where λ_a is the axial stretch and λ_t is the transverse stretch. The volumetric Hencky strain is $\varepsilon_v = \ln(\lambda_a \lambda_t^2) = \ln(\lambda_a) + 2\ln(\lambda_t) = \varepsilon_a + 2\varepsilon_t$. We can therefore compute the transverse strains readily if we know the volumetric and axial strains. In the case of hydrostatic compression we assume that there are no distortional strains and ignore the effect of anisotropy to get the relation $\varepsilon_v = 3\ln(\lambda)$ where $\lambda = \lambda_a = \lambda_t$. The equivalent Hencky strain is then given by

$$\varepsilon_{\text{eq}} = \begin{cases} \sqrt{(\ln\lambda_a)^2 + 2(\ln\lambda_t)^2} & \text{for uniaxial/triaxial compression} \\ \sqrt{3}\,\ln(\lambda) = \frac{1}{\sqrt{3}}\,\varepsilon_v & \text{for hydrostatic compression}\,. \end{cases} \tag{6}$$

3.6. *Shear tests*

For the shear tests on the PU foam, six blocks of dimensions 15 mm × 60 mm × 180 mm were machined from a foam panel. These blocks were oriented such that the long axis was either in direction 1 or direction 3. Figure 9 shows the orientation of the shear samples in the foam panel. The blocks were tested using the approach suggested in the test standard ASTM-C273/C273M-07a (2010). The foam could only be tested in the directions 1 (σ_{31}) and

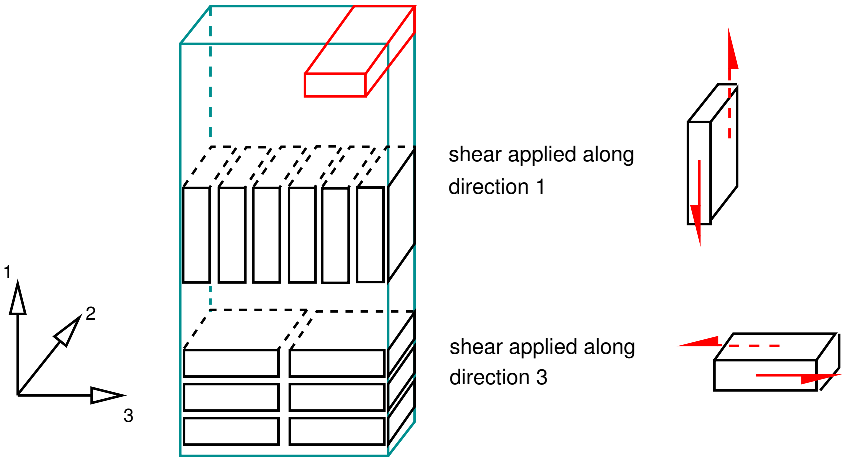

Figure 9: Orientation of shear test samples in a foam panel.

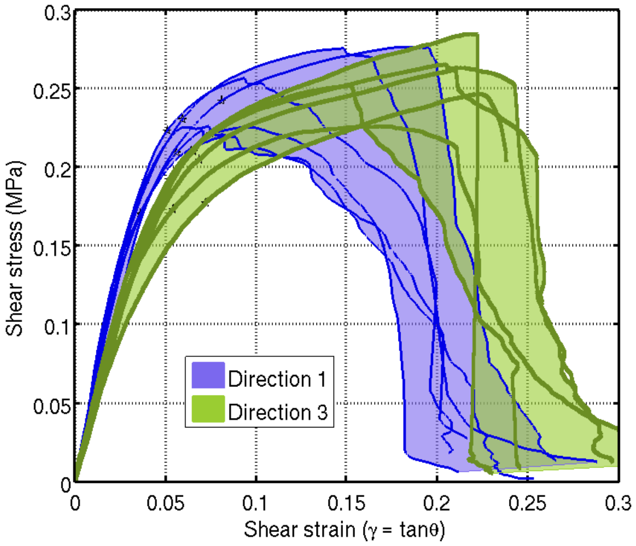

Figure 10: Stress-strain curves from shear tests on PU foam.

3 (σ_{13}) due to the specimen dimension requirements specified by the standard. The samples were loaded in tension along the long axis leading to a state of pure shear along the diagonal. A cross-head displacement rate of 0.8 mm per minute (strain rate of ~0.012 per second) was used for the tests.

The test is an approximation of simple shear with measurements being made with respect to a co-rotational coordinate. Plots of the true shear stress versus shear strain ($\gamma = \tan\theta$, where θ is the angle of shear) are shown in Figure 10. Table 5 lists the average shear properties of the PU foam in the 1–3 plane. In the table, ρ is the density, G is the shear modulus, σ_y is the true stress at initial yield, σ_{max} is the peak stress achieved, γ_y is the shear strain at initial yield, and γ_{max} is the shear strain at peak stress. Instead of the 2% offset strain being used to determine the yield point, the second derivative of each stress-strain curve was computed and the mid-point between of the local minimum and maximum in the second derivative was taken to be the yield point. It was also assumed that the volumes of the samples remained constant during the tests.

As expected, the shear behaviour of the foam in the 1–3 plane is largely independent of the direction of application of load. However, the samples loaded in direction 1 exhibited higher shear moduli and failed at lower strains

Table 5: Average shear properties of polyurethane foam in the 1-3 plane.

	ρ (kg/m^3)	G (MPa)	σ_y (MPa)	$\sigma_{\max}$ (MPa)	γ_y	$\gamma_{\max}$
Direction 1-3	42.83 ± 0.22	4.46 (± 10.13 %)	0.20 (± 8.93 %)	0.26 (± 8.31 %)	0.07 (± 11.42 %)	0.19 (± 14.63 %)
Direction 3-1	43.44 ± 0.23	5.68 (± 11.14 %)	0.22 (± 8.88 %)	0.25 (± 10.01 %)	0.06 (± 25.69 %)	0.12 (± 37.65 %)

than the samples loaded in direction 3. This can be attributed to the position in the panel from which the samples were machined. Similar behavior was observed in the compression and tension tests.

Equivalent shear strain. It is often convenient to use a logarithmic shear strain measure that is consistent with the logarithmic true strains used to characterize the tension and compression tests. For simple shear, the deformation gradient is given by

$$\boldsymbol{F} \equiv \begin{bmatrix} 1 & \gamma & 0 \\ 0 & 1 & 0 \\ 0 & 0 & 1 \end{bmatrix} \tag{7}$$

where $\gamma = \tan\theta$ is a simple shear deformation in the 1-direction and the 1–2 plane, and θ is the angle of shear. When we choose a Hencky logarithmic strain measure (either Lagrangian or Eulerian), an equivalent logarithmic strain measure that is appropriate for simple shear is (for more detail see Onaka (2012) and references listed in that paper)

$$\gamma_{\text{eq}} = \sqrt{2} \ln\left(\frac{\gamma}{2} + \sqrt{1 + \frac{\gamma^2}{4}}\right) . \tag{8}$$

This definition of the equivalent Hencky shear strain assumes that $\gamma_{\text{eq}} = \sqrt{\boldsymbol{\varepsilon}_{\text{iso}} : \boldsymbol{\varepsilon}_{\text{iso}}}$ where $\boldsymbol{\varepsilon}_{\text{iso}}$ is the isochoric (volume preserving) part of the Hencky strain $\boldsymbol{\varepsilon}$. An identical definition can be used for the equivalent plastic strain with γ replaced by the plastic shear deformation γ^p.

3.7. *Fracture toughness tests*

Single edge notch experiments based on the test standard ASTM-D5045-99 (2007) were performed to characterise the fracture behaviour of the PU foam in terms of the critical stress intensity factor (K_{Ic}) and the critical energy release rate (G_{Ic}). The test involves three point bending of a notched beam with a sharp crack at the tip of the notch. PU foam test samples were beams of dimensions 10 mm × 20 mm × 120 mm with a support span of 80 mm. A 2 mm wide and 5 mm deep notch was machined in the centre of the span of the beam with a band saw. The sharp crack was generated at the end of the notch by cutting the foam a further 5 mm with a sharp razor blade. All tests were performed at a uniform cross-head displacement rate of 10 mm per minute. An example of the notch and the crack at the end of the notch is shown in Figure 11.

Figure 12 shows the load-displacement behavior of the notched PU foam beams under three point bending. While there is some overlap between the curves for beams tested for mode I fracture toughness in direction 1 and those in direction 3, the average fracture toughness in direction 1 is higher than that in direction 3. However, the areas under the load displacement curves for both sets of samples are roughly identical.

The ASTM standard specifies some requirements of the load to failure for an edge notch test to be considered valid. Out of the 20 beams that were tested in direction 1, 15 samples satisfied these requirements while 13 of the 20 samples tested in direction 3 met the ASTM requirements. Table 6 lists the mean and the coefficient of variation of the results from the tests that are considered acceptable under the ASTM standard. The table also lists the maximum recorded load ($P_{\max}$) and the fracture energy (U_f), i.e., the integral of the load-displacement curve from zero load to $P_{\max}$. The critical mode I stress intensity factor (K_{Ic}) in direction 1 was noticeably larger than in direction 3. The ratio of K_{Ic} between direction 1 and 3 is approximately 1.43. This anisotropy is the result of the higher resistance

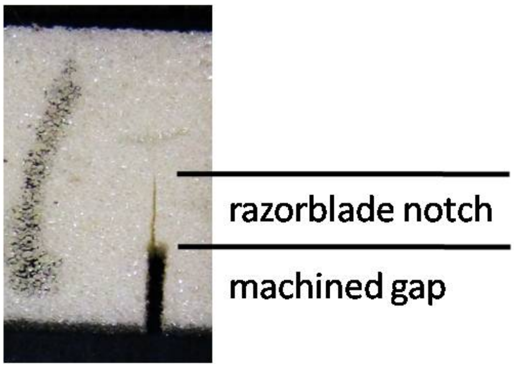

Figure 11: Magnified view of a foam sample containing an edge notch with a sharp crack at the end.

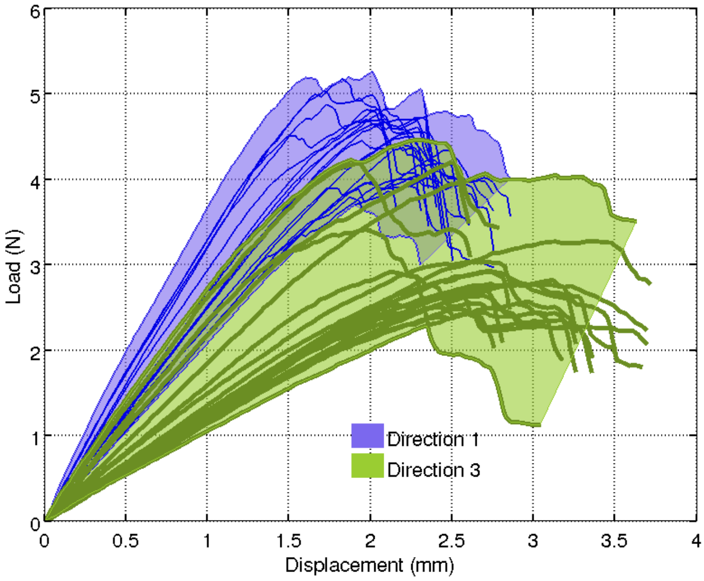

Figure 12: Load-displacement curves for edge notched PU beams under three-point bending.

Table 6: Average mode I fracture properties in directions 1 and 3. The numbers inside round brackets are the coefficients of variation expressed as percentages.

	K_{Ic} (kPa-m$^{1/2}$)	G_{Ic} (J/m^2)	$P_{\max}$ (N)	U_f (mJ)
Direction 1	37.2 (± 11.7 %)	106.4 (± 18.0 %)	4.6 (± 11.3 %)	5.0 (± 17.9 %)
Direction 3	26.0 (± 23.5 %)	97.6 (± 24.9 %)	3.2 (± 23.8 %)	4.6 (± 24.9 %)

to forces along the foam rise direction due to the elongated foam cell structure along that direction. Therefore the stress needed to propagate a crack is higher in direction 1 than it is in directions 2 and 3. In contrast to K_{Ic}, the critical energy release rates (G_{Ic}) have similar magnitudes in both directions. Therefore the anisotropy of the material does not appear to play an important role in determining the energy release rate. The material that actually fractures is the polyurethane of the cell walls which has similar properties in all directions. Therefore, G_{Ic} is related to the amount of PU material that is fractured per unit area of the crack. Since the amount of material in the cells walls is roughly identical in both directions the effective G_{Ic} of the foam is similar in both directions.

The relative size of the test samples is small compared to the cell size of the foam. Therefore, variability in the cell structure or the presence of small defects and flaws influences the fracture toughness quite dramatically. This is reflected in the high coefficients of variation shown in Table 6. Also, due to the cellular structure of the test samples, a mathematically sharp crack tip cannot be created and the crack tip is usually at a random location relative to a foam cell. The fracture toughness and strain energy release rate are strongly affected by the shape and location of the crack tip and this effect also contributes to the variability observed in the tests.

The ratio of the mean critical stress intensity factors in directions 1 and 3 is $\sim$1.4 which is identical to the shape anisotropy ratio observed in the tension and compression tests. This ratio and the structure-property relations in Gibson and Ashby (1999) provide an estimate the critical stress intensity factor in direction 2, which we find to be $K_{Ic} \sim 0.022$ MPa-m$^{1/2}$. Note that the observed value of the shape anisotropy ratio from the fracture toughness tests provides added confidence in our specimen preparation and test procedures.

4. Material models

The highly anisotropic and nonlinear nature of the PU foam makes constitutive modeling of the material a challenge. In this work we develop and use simplified models that attempt to represent the major features of the mechanical behavior of the material. These materials models include elasticity models, plasticity models (including flow stress, hardening, and candidate non-associated flow rules), but not damage criteria and the evolution of softening behavior. Temperature and strain rate can be important in determining the response of polymeric foams but are avoided in this study. Though our focus is on foam of a particular density, the models discussed in this paper can be extended to other foam densities by the application of transformations suggested in Gibson and Ashby (1999) and Daniel and Cho (2011).

If we are to derive an anisotropic hyperelastic strain energy potential that relates the Cauchy stress ($\boldsymbol{\sigma}$) to the Hencky strain[5], we need a suitable invariant basis for the Hencky strain. Such bases exist for isotropic materials (e.g.,Criscione et al. (2000)) and for special classes of anisotropy (e.g., Criscione et al. (2001)). Instead we use the hypoelastic approach with the equality of the rate of deformation tensor and the logarithmic rate of the Hencky strain (Xiao et al., 1997) as justification[6]. A detailed description of finite elastoplasticity in a Hencky strain framework can be found in Arghavani et al. (2011).

4.1. Elasticity model

For simplicity, we ignore all nonlinearities other than the dependence of the Poisson's ratio on the applied strain, and assume that the material is linear hypoelastic prior to plastic deformation. Changes in elastic moduli and the evolution of the principal axes of anisotropy (eigentensors of the elastic stiffness tensor) due to void collapse during compression and other elastic-plastic coupling effects are ignored[7] We also assume that the PU foam is transversely isotropic and that elastic moduli in tension and compression are identical.

Histograms of the elastic moduli determined from the characterization tests are compared in Figure 13. The plot shows the mean values and the error bars represent the 95% confidence interval around the expected value assuming a Gaussian distribution. The difference between the tensile and compressive moduli suggests a degree of nonlinearity in the elastic response, a fact also observed in the stress-strain curves for the PU foam. The elastic moduli in directions 2 (E_{22}) and 3 (E_{33}) are nearly identical. The shear modulus in the 1–3 plane also has an expected value that falls within the range of variation of E_{22} and E_{33}.

The expected value of E_{11} is taken to be mean of the compressive and tensile moduli in direction 1. The mean of all the tensile and compressive moduli in directions 2 and 3 is taken to be the expected value of $E_{22} = E_{33}$.

---

[5] The Hencky strain can either be expressed in Lagrangian form ($\ln \boldsymbol{U}$) or in Eulerian form ($\ln \boldsymbol{V}$), where $\boldsymbol{U}$ and $\boldsymbol{V}$ are the right and left stretch tensors, respectively. We choose the later for consistency.

[6] The use of the logarithmic rate as an objective rate for the Cauchy stress is problematic because it is not the Lie derivative of any stress like quantity. Other objective rates could be substituted as long as the material model calibration explicitly takes that rate into consideration.

[7] These issues are important. Micromechanical modeling can be used to extend the models in this paper to include elastic-plastic coupling.

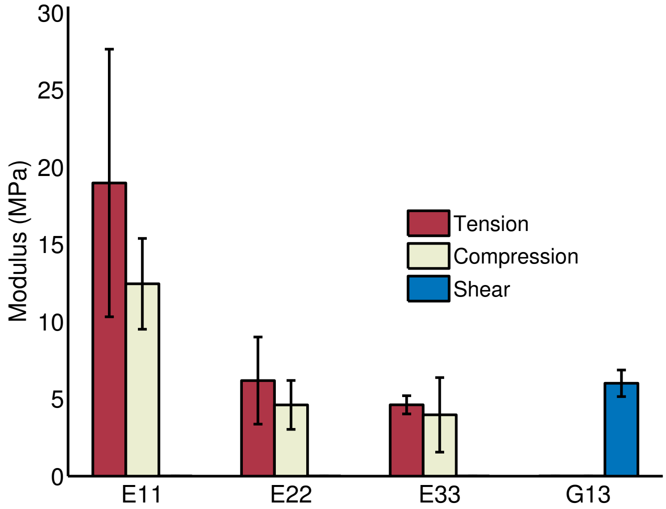

Figure 13: Mean elastic moduli with 95% confidence intervals.

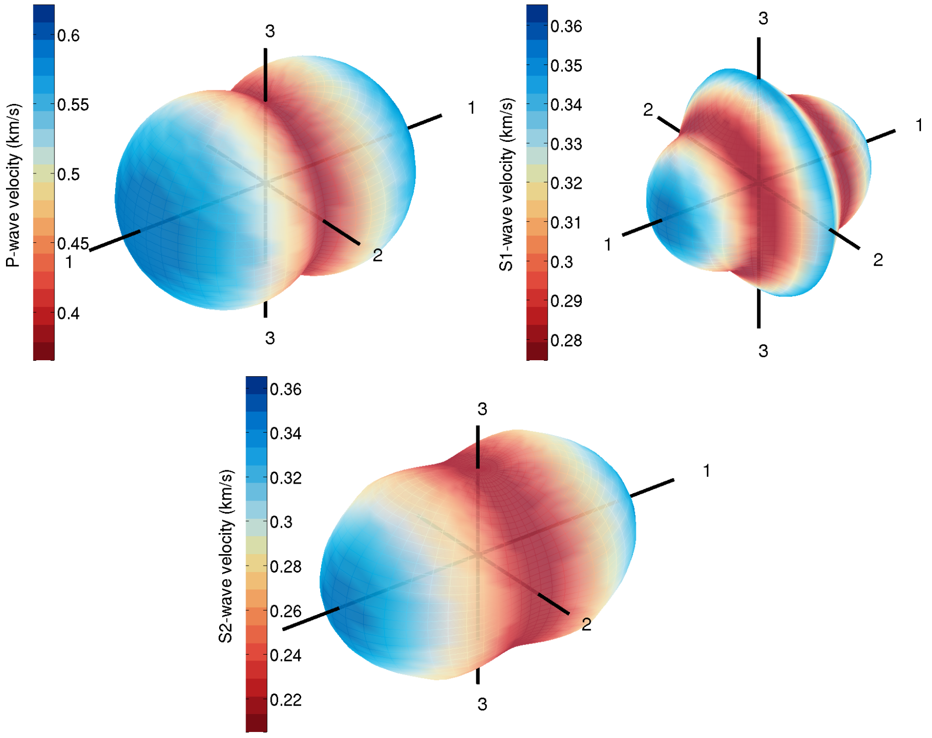

Figure 14: Anisotropy in the three wave velocities in the PU foam.

The Poisson's ratios ν_{23}, ν_{12}, and ν_{13} are assumed to be 0.3 for small strains. Using the 95% confidence intervals around these expected values, a 2^3 factorial design set was used to compute the remaining shear modulus (G_{23}), the Poisson's ratios ($\nu_{21} = \nu_{31}$), the stiffness matrix ($\mathbf{C}$), the shape-anisotropy ratio (R) (Gibson and Ashby, 1999, p. 260), the universal anisotropy index (A) (Ranganathan and Ostoja-Starzewski, 2008), and their confidence intervals.

The anisotropy in the three principal wave velocities of the PU foam computed from the mean stiffness tensor is depicted in Figure 14. The P-wave velocity varies between ∼400 m/s in the 2–3 plane to ∼600 m/s in direction 1. The fast shear wave (S1) has its peaks (∼360 m/s) in the 2–3 plane and in direction 1 and its minimum at an inclination of 30° to the 2–3 plane. The slow shear wave (S2) has a minimum of ∼ 200 m/s in the 2–3 plane and a maximum of 360 m/s in direction 1.

Table 7 lists the expected values and the 95% confidence bounds on the elastic properties and elastic anisotropy of the PU foam. The anisotropy ratio ($A = 2.26$) is relatively high and suggests that the usual assumption of isotropy for PU foams may lead to misleading predictions in numerical simulations. If we use the shape-anisotropy ratio (R) to compute the shear modulus in the 2–3 plane using relation suggested in (Gibson and Ashby, 1999, eq. (6.31)), we get $G_{23} \sim 7.2$ MPa which is higher than $E_{22} = E_{33}$ and also leads to a Poisson's ratio ν_{23} of -0.65 which is not observed in our experiments on the PU foam.

Table 7: Elastic properties of PU foam with 95% confidence bounds. Note that only five of these moduli are independent.

E_{11} (MPa)	$E_{22} = E_{33}$ (MPa)	$\nu_{12} = \nu_{13}$	$\nu_{21} = \nu_{31}$	$\nu_{23} = \nu_{32}$	G_{23} (MPa)	$G_{12} = G_{13}$ (MPa)
16^{+3}_{-3}	$4.9^{+0.6}_{-0.6}$	0.3	$0.096^{+0.034}_{-0.029}$	0.3	$1.9^{+0.2}_{-0.2}$	$6^{+0.4}_{-0.4}$

C_{11} (MPa)	$C_{12} = C_{13}$ (MPa)	C_{22} (MPa)	C_{23} (MPa)	C_{44} (MPa)	$C_{55} = C_{66}$ (MPa)	
$17.4^{+3.3}_{-3.3}$	$2.3^{+0.4}_{-0.4}$	$5.7^{+0.9}_{-0.8}$	$1.9^{+0.4}_{-0.3}$	$1.9^{+0.2}_{-0.2}$	$6.0^{+0.4}_{-0.4}$	

A	R	
$2.26^{+1.12}_{-0.98}$	$1.41^{+0.18}_{-0.17}$	

Uniaxial compression tests indicate that the Poisson's ratios of the foam rapidly approach zero as deformation continues. A simple model for this behavior is given by equations (2) where the strain ε can be interpreted as the maximum principal strain.

4.2. Plasticity model

Plasticity models for foams and porous solids have a long history and numerous phenomenological models have been suggested on the basis of empirical or micromechanical reasoning (Gibson et al., 1982; Gibson and Ashby, 1982; Maiti et al., 1984). Foam models usually assume an ellipsoidal yield surface (e.g., Schreyer et al. (1994); Zhang et al. (1998); Deshpande and Fleck (2000, 2001); Hanssen et al. (2002); Combaz et al. (2010)) and a nonassociated flow rule postulated on the basis of the observation that transverse plastic strains are not observed in uniaxial compression tests. Hardening models are usually determined experimentally. Our experimental data on PU foams do not fit any existing, sufficiently-smooth, foam models we are aware of.

However, soil and geomaterial models are potential candidates (see, for example, the variations on the Cam-clay model listed in Ling et al. (2002)). Most existing geomaterial models are inadequate for the computational modeling of foams because tensile strength is neglected and discontinuous caps are used to bound the yield surface. We seek a single smooth yield surface that can capture both the tensile behavior of PU foam and the compression cap. The process of devising such a surface is described below. Note that our yield surface is general enough to capture a large range of plastic phenomena.

The difficulty of determining the form of the flow rule (particularly for non-associated plastic flow) has led a number of authors to suggest that both the yield surface and the flow rule be derived from thermodynamic considerations starting with a dissipation function (Collins and Houlsby, 1997; Houlsby, 2003). If, in addition, we use a dilatation model that exhibits the correct plastic Poisson's effect (e.g., Chandler and Sands (2010); Sands and Chandler (2010)) we can derive both yield surfaces and flow rules that behave in a consistent manner. However, we have found that the process of fitting the experimental data to a model is complicated if we follow the approach suggested by Chandler and Sands (2010).

In this paper we consider only rate-independent plasticity and ignore strain-rate effects. Because of lack of experimental data, we also ignore the potential dependence of the yield stress on J_3 (the third principal invariant of the deviatoric Cauchy stress) which has been found to be necessary for phenomenological plasticity models to reproduce experimental data under multiaxial loading (see, for example, Pivonka and Willam (2003); McElwain et al. (2006)).

4.2.1. Yield surface

Figure 15(a) depicts the stress difference $\sigma_1 - \sigma_3$[8] (often called the stress deviator in the geomechanics literature) as a function of the mean stress (p) at initial yield and at various stages of hardening. The filled blue circles in the figure indicate the state at initial yield. The solid blue line is an elliptical curve fit to the initial yield data on the top half of the plot. The dashed magenta line is a piriform curve fit to the data for a volumetric plastic strain of 1.2. These curve indicate that there is a significant amount of flattening of the initial yield surface as plastic deformation progresses. The data in the bottom half of the plot are more difficult to fit, primarily because the triaxial tests show yielding at much lower values of stress than the shear tests and uniaxial tensions tests.

The plot in Figure 15(b) shows a scaled version of Figure 15(a) in which the Cauchy stress tensor ($\boldsymbol{\sigma}$) has been transformed to a scaled stress tensor ($\bar{\boldsymbol{\sigma}}$) using the linear transformation

$$\bar{\boldsymbol{\sigma}} = \mathbf{T} : \boldsymbol{\sigma} \implies \begin{bmatrix} \bar{\sigma}_{11} \\ \bar{\sigma}_{22} \\ \bar{\sigma}_{33} \\ \bar{\sigma}_{23} \\ \bar{\sigma}_{31} \\ \bar{\sigma}_{12} \end{bmatrix} = \begin{bmatrix} 1 & 0 & 0 & 0 & 0 & 0 \\ 0 & R & 0 & 0 & 0 & 0 \\ 0 & 0 & R & 0 & 0 & 0 \\ 0 & 0 & 0 & R & 0 & 0 \\ 0 & 0 & 0 & 0 & \sqrt{(1+R+R^2)/3} & 0 \\ 0 & 0 & 0 & 0 & 0 & \sqrt{(1+R+R^2)/3} \end{bmatrix} \begin{bmatrix} \sigma_{11} \\ \sigma_{22} \\ \sigma_{33} \\ \sigma_{23} \\ \sigma_{31} \\ \sigma_{12} \end{bmatrix} \tag{9}$$

where $\mathbf{T}$ is a symmetric fourth-order tensor and R is the shape-anisotropy ratio[9]. The scaled stress deviator ($\bar{q}$) and the scaled mean stress ($\bar{p}$) are defined as

$$\begin{aligned} \bar{p} &= \tfrac{1}{3}\,\mathrm{tr}(\bar{\boldsymbol{\sigma}}) = \tfrac{1}{3}\bar{I}_1 = \tfrac{1}{3}(\sigma_{11} + R\sigma_{22} + R\sigma_{33}), \quad \text{and} \\ \bar{q} &= \sqrt{\tfrac{3}{2}\bar{s} : \bar{s}} = \sqrt{3\bar{J}_2} \\ &= \sqrt{\tfrac{1}{2}\left[(\sigma_{11} - R\sigma_{22})^2 + R^2(\sigma_{22} - \sigma_{33})^2 + (R\sigma_{33} - \sigma_{11})^2\right] + 3R^2\sigma_{23}^2 + (1+R+R^2)(\sigma_{31}^2 + \sigma_{12}^2)} \end{aligned} \tag{10}$$

where $\bar{s} = \bar{\boldsymbol{\sigma}} - 1/3\,\mathrm{tr}(\bar{\boldsymbol{\sigma}})\,\boldsymbol{1}$ is the deviatoric part of $\bar{\boldsymbol{\sigma}}$. The above expressions reduce to the usual definitions of p and q for the isotropic case where $R = 1$. Similar scaled stresses have been justified on the basis of micromechanical considerations by Alkhader and Vural (2010). The upper half of the $\bar{p} - \bar{q}$ space shows yield stresses from experiments where the dominant stress was in the rise direction while the lower half shows yield stresses from tests where the primary load was applied in the transverse 2-3 plane. From the uniaxial compression results shown in Figure 15(a)

---

[8] The convention that compression is positive is used in Figure 15(a). The quantity σ_1 represents the stress in direction 1 which is not necessarily the maximum principal stress. The quantity σ_3 represents stresses in the 2–3 plane (assuming isotropy in that plane). The positive $\sigma_1 - \sigma_3$ half space in the figure contains data points for uniaxial compression in direction 1, triaxial compression where $\sigma_1 > \sigma_3$, uniaxial tension in directions 2 and 3, and simple shear in direction 1 in the 1–3 plane. The negative half-space in the figure includes uniaxial compression data in the 2–3 plane (including directions 2 and 3 and intermediate orientations), uniaxial tension in direction 1, and simple shear in direction 3 in the 1–3 plane.

[9] The expression for $\mathbf{T}$ is the simplest that can be used to describe the data. More complex forms may be used if needed. For example, if the yield surface is orthotropic we can use two scaling parameters R_2 and R_3 instead of R

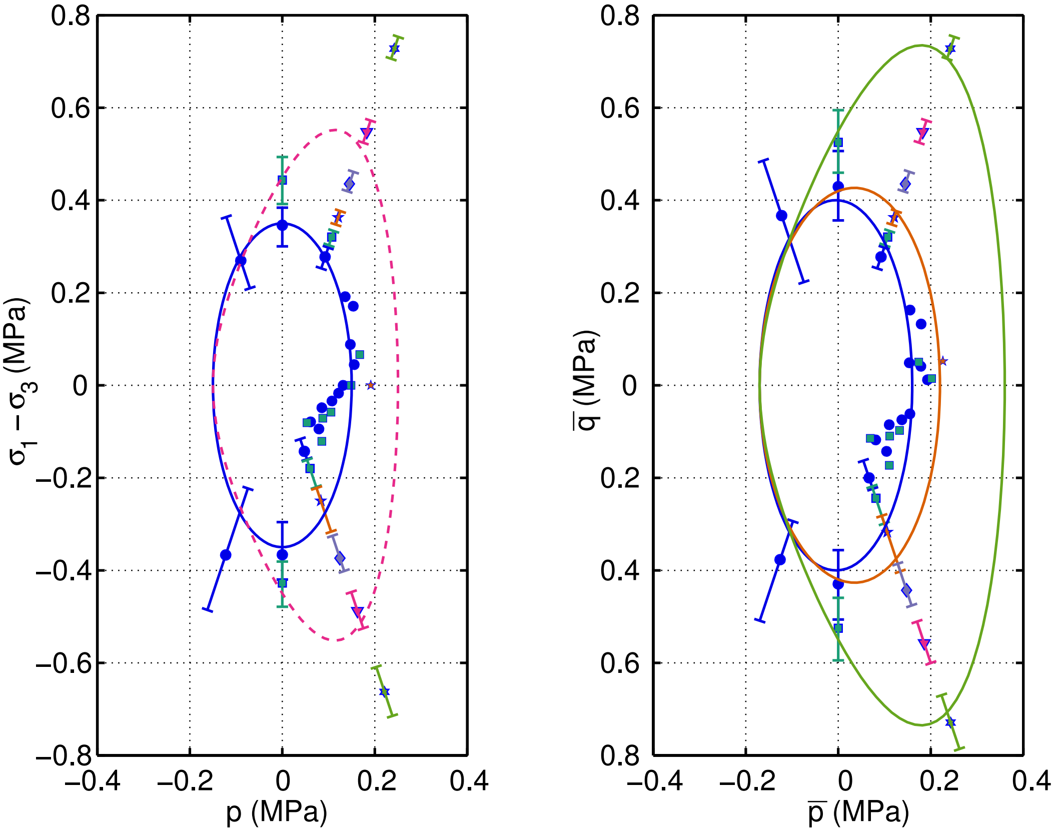

(a) Unscaled stresses.

(b) Scaled stresses.

Figure 15: (a) Stress difference ($\sigma_1 - \sigma_3$) as a function of the mean stress (p). (b) Scaled deviatoric and mean stresses at yield and at various stages of hardening. The symbols $\circ$, $\square$, $\star$, $\diamond$, and $\triangle$ indicate the state at equivalent plastic strains of 0, 0.2, 0.6, 1.0, and 1.2, respectively. The hexagrams indicate a strain of 1.4. The error bars indicate a 95% confidence interval around the mean value. The closed curves depict the postulated shape of the yield surface at various stages of deformation.

it can be observed that the anisotropy in the yield stress decreases as the plastic strain increases. The scaled plot takes this effect into consideration by assuming

$$R(\varepsilon^p_{\text{eq}}) = 1.0 + R_0 \exp(-R_1\, \varepsilon^p_{\text{eq}}) \tag{11}$$

where $\varepsilon^p_{\text{eq}}$ is the equivalent plastic strain[10] with $R_0 = 0.4$ and $R_1 = 1.0$. This equation can be interpreted as an evolution rule for a simplified fabric tensor of the material. The initial ellipsoidal yield surface in scaled space fits the experimental data better and evolves into a piriform surface with progressive deformation. Empirically, the test data point to a yield surface that is initially ellipsoidal but evolves into a surface that becomes flatter in the compression cap region. The micromechanics of this behavior are unclear and requires further investigation.

To represent the observed yield behavior of the foam with a single yield surface, we start with an initial ellipsoid and map it to a piriform shape. Let the initial yield surface be described in by the ellipse

$$\left(\frac{\bar{q}}{\bar{q}_s}\right)^2 + \left(\frac{\bar{p}}{\bar{p}_c}\right)^2 = 1\,. \tag{12}$$

where $\bar{p}_c$ and $\bar{q}_s$ are material constants. In parametric form, the yield surface can be expressed as

$$\bar{p} = \bar{p}_c \cos\theta\,,\quad \bar{q} = \bar{q}_s \sin\theta \qquad \theta \in [0,\pi] \tag{13}$$

where θ is a parameter. We want to map this ellipse ($X = A\cos\theta, Y = B\sin\theta$) to a piriform described by

$$x = a\,(1 + \alpha\cos\theta)\,,\quad y = b\,(1 + \beta\cos\theta)\sin\theta \qquad \theta \in [0,\pi] \tag{14}$$

where a, b, α, and β are constants. The deformed ellipse has to be translated by a factor of $2A$ so that it matches the original ellipse, i.e, $x = a(1 + \alpha\cos\theta) - 2A$. To match the ellipse to the piriform at $\theta = \pi$ and $\theta = \pi/2$ we need $a = A/(1-\alpha)$ and $b = B$. Additionally, to match the two curves at $\theta = 0$ we need $\alpha = 1/2$. Smaller values of $\alpha \in (0,1)$ shrink the piriform along the x-axis while larger values increase the size along that axis. With these values of a and α, the piriform matches the ellipse exactly for $\beta = 0$ and becomes skewed as $\beta \in [0,1]$ increases.

To achieve the desired shape of the yield function, the shifted piriform curve has to be scaled so that the mean stress at failure in equitriaxial tension remains unchanged with plastic deformation. If the value of A for equitriaxial tension is A_0, a linear interpolation between A and A_0 can be used to scale the piriform. The resulting expression for the curve is

$$x = \left[\frac{A(\pi-\theta) + A_0\theta}{\pi}\right]\left[\frac{\alpha(2+\cos\theta) - 1}{1-\alpha}\right]\,,\quad y = B\,(1 + \beta\cos\theta)\sin\theta \qquad \theta \in [0,\pi]\,. \tag{15}$$

However, conversion of the above expression into the non-parametric form convenient for return algorithms is non-trivial and a translation of the curve by $A - A_0$ is simpler. In that case, the parametric form of the piriform curve (with $\alpha = 1/2$) is

$$\frac{x + A_0}{A} = 1 + \cos\theta\,,\quad \frac{y}{B} = (1 + \beta\cos\theta)\sin\theta\,. \tag{16}$$

Combining these gives us the expression for the four-parameter yield surface (with the substitutions $x \to \bar{p}, y \to \bar{q}, A \to \hat{p}_c, B \to \hat{q}_s, A_0 \to \bar{p}_t$)

$$\left(\frac{\bar{q}}{\hat{q}_s}\right)^2 + \left[\beta\left(\frac{\bar{p} + \bar{p}_t}{\hat{p}_c} - 1\right) + 1\right]^2 \left(\frac{\bar{p} + \bar{p}_t}{\hat{p}_c} - 2\right)\left(\frac{\bar{p} + \bar{p}_t}{\hat{p}_c}\right) = 0\,. \tag{17}$$

Due to the translation of the yield surface, the quantities $\hat{p}_c$ and $\hat{q}_s$ no longer represent the scaled yield stress in equitriaxial compression ($\bar{p}_c$) and pure shear ($\bar{q}_s$), respectively. The intersections of the yield surface with the $\bar{p}$ and $\bar{q}$ axes give us the relations we need:

$$\hat{p}_c = \frac{\bar{p}_c + \bar{p}_t}{2} \quad \text{and} \quad \hat{q}_s = \bar{q}_s\left[\frac{(\bar{p}_c + \bar{p}_t)^2}{2\sqrt{\bar{p}_c\bar{p}_t}\,\left[(1-\beta)\bar{p}_c + (1+\beta)\bar{p}_t\right]}\right]\,. \tag{18}$$

---

[10] The equivalent plastic strain is defined in equation (30) and reasons for the particular form used in this paper are discussed in Section 4.2.2.

The yield surface described by equation (17) can be algebraically simplified to

$$\boxed{f := \left(\frac{\bar{q}}{\bar{q}_s}\right)^2 - \left(1 - \frac{\bar{p}}{\bar{p}_c}\right)\left(1 + \frac{\bar{p}}{\bar{p}_t}\right)\left[1 + \frac{2\beta\,\bar{p}}{(1-\beta)\,\bar{p}_c + (1+\beta)\,\bar{p}_t}\right]^2 = 0\,.} \tag{19}$$

The internal variables that evolve during plastic deformation are the anisotropy ratio (R), the yield stress in equi-triaxial compression ($\bar{p}_c$), the yield stress in shear ($\bar{q}_s$), and the yield surface shape factor (β). We assume that the yield stress in hydrostatic tension ($\bar{p}_t$) remains constant.

Figure 16 shows plots of the initial (ellipsoidal) and hardened (piriform) yield surfaces in principal stress space. As before, compression is positive and we have assumed that the principal stresses are aligned with the principal material directions. In the tension regime, the yield surface shrinks slightly with increasing plastic deformation as the shape moves from ellipsoidal to piriform. The π-plane traces of the yield surface shown in Figure 16(b) are elliptical. Our experimental data are insufficient to determine whether a triangular shape is more appropriate. The 1–2 plane traces of the yield surface in Figure 16(c) show the anisotropy in direction 1 while the traces in the 2–3 plane (Figure 16(d)) show that the yield surface is isotropic in that plane.

Contours of the yield function (19) in $\bar{p} - \bar{q}$ space are shown in Figure 17. The yield function is negative inside the zero level set which is indicated by a dashed line in the figure. There is a local maximum near the triaxial tension region of stress space that has the potential to cause Newton root finding algorithms used in plasticity algorithms to converge to the wrong solution. Special care has to be exercised when trial stress states are in the tension regime. However, the extent of the non-convex region is significantly smaller and less problematic than in most closed, non-ellipsoidal, yield functions in the literature.

The normal to the yield surface in unscaled stress space is given by

$$\boldsymbol{N} = \frac{\partial f}{\partial \boldsymbol{\sigma}} = \frac{\partial f}{\partial \bar{\boldsymbol{\sigma}}} : \frac{\partial \bar{\boldsymbol{\sigma}}}{\partial \boldsymbol{\sigma}} = \mathbf{T} : \frac{\partial f}{\partial \bar{\boldsymbol{\sigma}}} \tag{20}$$

due to the symmetry of $\mathbf{T}$. The normal to the yield surface in scaled stress space can be expressed as

$$\frac{\partial f}{\partial \bar{\boldsymbol{\sigma}}} = \frac{\partial f}{\partial \bar{p}}\frac{\partial \bar{p}}{\partial \bar{\boldsymbol{\sigma}}} + \frac{\partial f}{\partial \bar{q}}\frac{\partial \bar{q}}{\partial \bar{\boldsymbol{\sigma}}}\,. \tag{21}$$

The derivatives of $\bar{p}$ and $\bar{q}$ with respect to the scaled stress ($\bar{\boldsymbol{\sigma}}$) have the standard forms

$$\frac{\partial \bar{p}}{\partial \bar{\boldsymbol{\sigma}}} = \frac{1}{3}\frac{\partial \bar{I}_1}{\partial \bar{\boldsymbol{\sigma}}} = \frac{1}{3}\boldsymbol{1} \quad \text{and} \quad \frac{\partial \bar{q}}{\partial \bar{\boldsymbol{\sigma}}} = \frac{\sqrt{3}}{2\sqrt{\bar{J}_2}}\frac{\partial \bar{J}_2}{\partial \bar{\boldsymbol{s}}} : \frac{\partial \bar{\boldsymbol{s}}}{\partial \bar{\boldsymbol{\sigma}}} = \frac{3}{2}\frac{\bar{\boldsymbol{s}}}{\bar{q}} = \sqrt{\frac{3}{2}}\frac{\bar{\boldsymbol{s}}}{\lVert\bar{\boldsymbol{s}}\rVert} \tag{22}$$

The derivatives of the yield function with respect to $\bar{p}$ and $\bar{q}$ are

$$\begin{aligned}\frac{\partial f}{\partial \bar{p}} = &\left[1 + \frac{2\beta\bar{p}}{(1-\beta)\bar{p}_c + (1+\beta)\bar{p}_t}\right] \times \\ &\left[\frac{(2\bar{p} - \bar{p}_c + \bar{p}_t)(\bar{p}_c + \bar{p}_t) + \beta\left[8\bar{p}(\bar{p} - \bar{p}_c + \bar{p}_t) + \bar{p}_c^2 + \bar{p}_t^2 - 6\bar{p}_c\bar{p}_t\right]}{\bar{p}_c\bar{p}_t\left[(1-\beta)\bar{p}_c + (1+\beta)\bar{p}_t\right]}\right]\end{aligned} \tag{23}$$

and

$$\frac{\partial f}{\partial \bar{q}} = \frac{2\bar{q}}{\bar{q}_s^2} \quad \implies \quad \frac{\partial f}{\partial \bar{q}}\frac{\partial \bar{q}}{\partial \bar{\boldsymbol{\sigma}}} = \frac{3\bar{\boldsymbol{s}}}{\bar{q}_s^2}\,. \tag{24}$$

For the case where $\beta = 0$, we have

$$f = \left(\frac{\bar{q}}{\bar{q}_s}\right)^2 - \left(1 - \frac{\bar{p}}{\bar{p}_c}\right)\left(1 + \frac{\bar{p}}{\bar{p}_t}\right) \quad \text{and} \quad \frac{\partial f}{\partial \bar{p}} = \frac{2\bar{p} - \bar{p}_c + \bar{p}_t}{\bar{p}_c\bar{p}_t}\,. \tag{25}$$

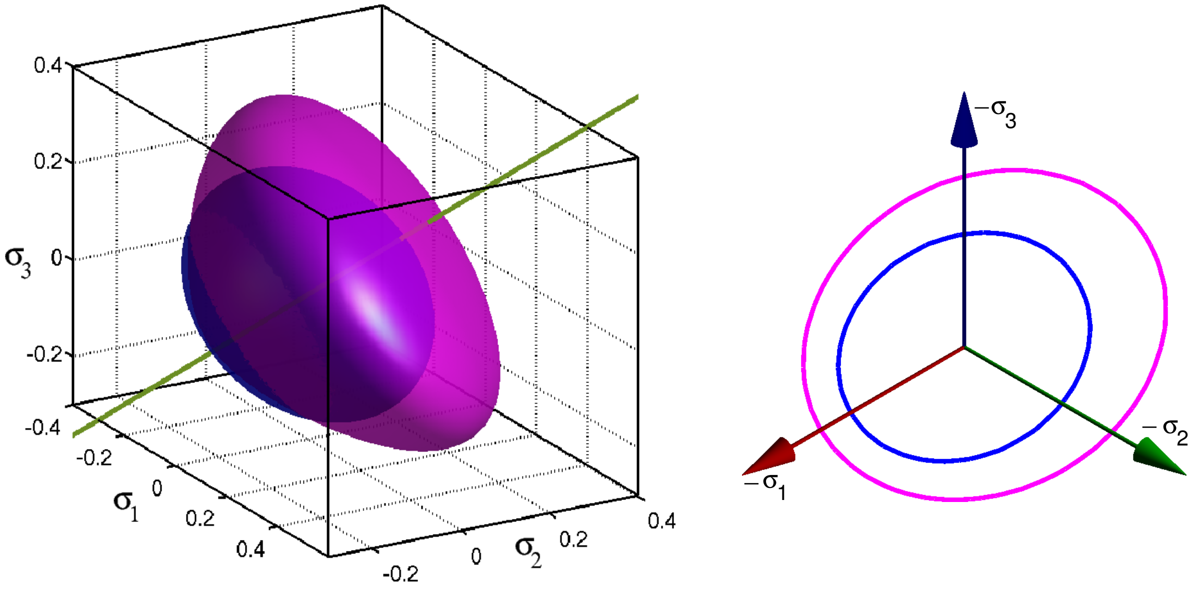

(a) Three-dimensional representation of yield surfaces.

(b) Yield surfaces in the π-plane.

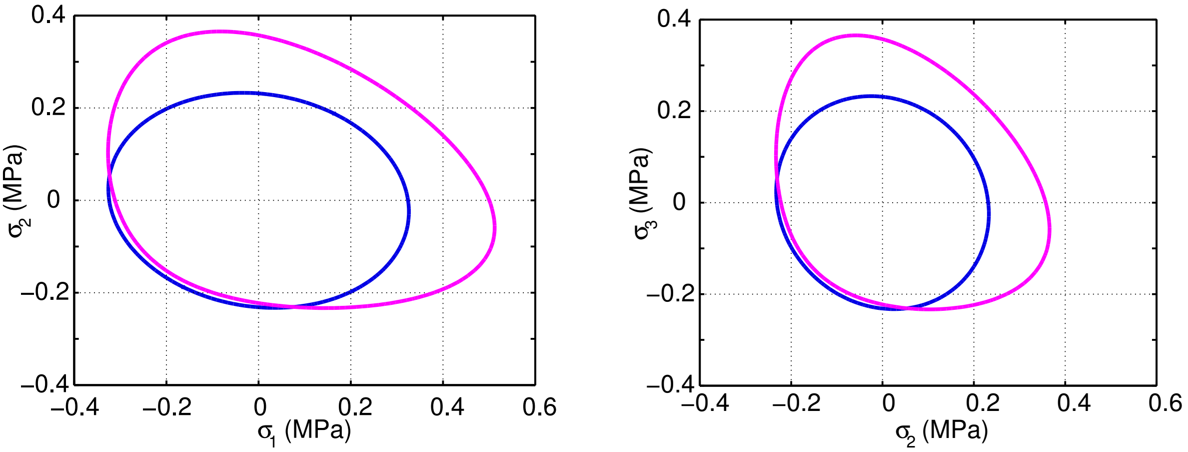

(c) Yield surfaces in the 1–2 and 1–3 planes.

(d) Yield surfaces in the 2–3 plane.

Figure 16: Yield surfaces in principal stress space where σ_1 is aligned with the rise direction and σ_2, σ_3 are in the transverse plane. The blue surface is at initial yield and the magenta surface is at a volumetric plastic strain of 1.2. For the blue ellipsoidal surface $\bar{p}_c = \bar{p}_t = 0.17$ MPa, $\bar{q}_s = 0.42$ MPa, and $\beta = 0$. For the magenta surface, $\bar{p}_t = 0.17$ MPa, $\bar{p}_c = 0.22$ MPa, $\bar{q}_s = 0.6$ MPa, and $\beta = 0.4$. The value of the stress anisotropy ratio R is 1.4.

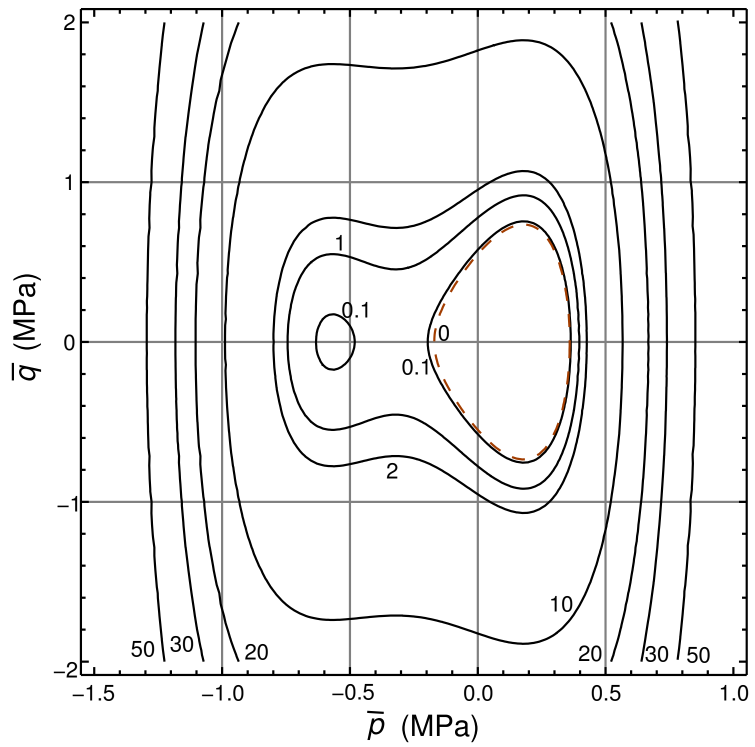

Figure 17: Isovalue contours of the yield function (19) in $\bar{p}-\bar{q}$ space for parameters $\bar{p}_t$=0.17 MPa, $\bar{p}_c$=0.36 MPa, $\bar{q}_s$=0.55 MPa, and β=0.4. The dashed curve shows the yield surface (zero level set).

For the case where $\bar{p}_c = \bar{p}_t$ and $\beta \neq 0$, we have

$$f = \left(\frac{\bar{q}}{\bar{q}_s}\right)^2 + \left[\left(\frac{\bar{p}}{\bar{p}_c}\right)^2 - 1\right]\left(1 + \frac{\beta\bar{p}}{\bar{p}_c}\right)^2 \quad \text{and} \quad \frac{\partial f}{\partial \bar{p}} = \frac{2}{\bar{p}_c}\left(1 + \frac{\beta\bar{p}}{\bar{p}_c}\right)\left[2\beta\left(\frac{\bar{p}}{\bar{p}_c}\right)^2 + \frac{\bar{p}}{\bar{p}_c} - \beta\right] \tag{26}$$

For the case where $\bar{p}_c = \bar{p}_t$ and $\beta = 0$, we have

$$f = \left(\frac{\bar{q}}{\bar{q}_s}\right)^2 + \left(\frac{\bar{p}}{\bar{p}_c}\right)^2 - 1 \quad \text{and} \quad \frac{\partial f}{\partial \bar{p}} = \frac{2\bar{p}}{\bar{p}_c^2}\,. \tag{27}$$

4.2.2. Flow rule

The flow rule for rate-independent plasticity can be written in the form

$$\overset{\circ}{\boldsymbol{\varepsilon}}{}^p = \dot{\lambda}\,\boldsymbol{P}$$

where $\overset{\circ}{\boldsymbol{\varepsilon}}{}^p$ is an objective inelastic strain rate, $\dot{\lambda}$ is a scalar multiplier, and $\boldsymbol{P}$ is an admissible rank 2 tensor valued function that satisfies thermodynamical consistency (see, for example, Acharya and Shawki (1996); Collins and Houlsby (1997); Bertram and Krawietz (2012) for possible consistency constraints). The function $\boldsymbol{P}$ can be specified by assuming the existence of a smooth convex dissipation potential (Π_p) such that

$$\overset{\circ}{\boldsymbol{\varepsilon}}{}^p = \dot{\lambda}\,\frac{\partial \Pi_p}{\partial \boldsymbol{\Sigma}} \qquad \text{where} \quad \boldsymbol{\Sigma} := -\frac{\partial \psi_h}{\partial \boldsymbol{\varepsilon}^p} = \frac{\partial \psi_g}{\partial \boldsymbol{\varepsilon}^p}$$

and ψ_h, ψ_g are the Helmholtz and Gibbs free energy functionals, respectively. For materials that do not have elastic-plastic coupling, the above relation can be simplified to(Collins and Houlsby, 1997)

$$\overset{\circ}{\boldsymbol{\varepsilon}}^p = \dot{\bar{\lambda}}\, \boldsymbol{P} = \dot{\bar{\lambda}}\, \frac{\partial \Pi_p}{\partial \boldsymbol{\sigma}}$$

i.e., $\boldsymbol{P}$ has a direction that is normal to the surface described by the dissipation potential. For rate-independent plasticity the Legendre dual of the dissipation potential can be identified as a function (g), similar to the yield function, that is identically zero for plastic states. Let us consider the case where the coordinate frame is chosen such that the rate of plastic strain is given by

$$\overset{\circ}{\boldsymbol{\varepsilon}}^p = \dot{\bar{\lambda}}\, \frac{\partial g}{\partial \boldsymbol{\sigma}} =: \dot{\bar{\lambda}} \boldsymbol{M} \quad \text{or} \quad \overset{\circ}{\boldsymbol{\varepsilon}}^p = \dot{\lambda}\, \frac{\partial g}{\partial \boldsymbol{\sigma}} \Big/ \left\| \frac{\partial g}{\partial \boldsymbol{\sigma}} \right\| =: \dot{\lambda} \hat{\boldsymbol{M}} \tag{28}$$

where $\overset{\circ}{\boldsymbol{\varepsilon}}^p$ is an objective strain rate, $\dot{\lambda} > 0$ is a scalar multiplier, $g \equiv g(\bar{p}, \bar{q}, p_c, q_c, \beta; \boldsymbol{\sigma}, \varepsilon^p)$ is a plastic potential, $\boldsymbol{M}$ is the normal to the plastic potential, and $\hat{\boldsymbol{M}}$ is the unit normal to the plastic potential. If the Eulerian Hencky strain ($\boldsymbol{\varepsilon}^p = \ln \boldsymbol{V}^p$) is taken to be the plastic strain measure, the objective rate is defined as (Bruhns et al., 1999; Xiao et al., 2006)

$$\overset{\circ}{\boldsymbol{\varepsilon}}^p = \dot{\boldsymbol{\varepsilon}}^p + \boldsymbol{\varepsilon}^p\, \Omega^{\log} - \Omega^{\log}\, \boldsymbol{\varepsilon}^p$$

where $\Omega^{\log}$ is the corotational logarithmic spin[11].

The normalized form of $\partial g / \partial \boldsymbol{\sigma}$ is needed for a definition of a scalar "consistent" plastic strain that is identical for all admissible potential functions, i.e., $\varepsilon^p_{\text{con}} := \lambda = \int \dot{\lambda}\, dt = \int ||\dot{\boldsymbol{\varepsilon}}^p||\, dt$, because

$$||\overset{\circ}{\boldsymbol{\varepsilon}}^p||^2 = \overset{\circ}{\boldsymbol{\varepsilon}}^p : \overset{\circ}{\boldsymbol{\varepsilon}}^p = (\dot{\lambda})^2 \left(\frac{\partial g}{\partial \boldsymbol{\sigma}} : \frac{\partial g}{\partial \boldsymbol{\sigma}} \right) \Big/ \left\| \frac{\partial g}{\partial \boldsymbol{\sigma}} \right\|^2 = \dot{\lambda}^2 \hat{\boldsymbol{M}} : \hat{\boldsymbol{M}} = \dot{\lambda}^2 \,. \tag{29}$$

For calibrating plasticity models with experimental data, it is convenient to use an equivalent "total" plastic strain (or, alternatively, the plastic work) defined as

$$\varepsilon^p_{\text{eq}} := ||\boldsymbol{\varepsilon}^p|| = \sqrt{\boldsymbol{\varepsilon}^p : \boldsymbol{\varepsilon}^p} \,. \tag{30}$$

The time derivative of this quantity is given by

$$\dot{\varepsilon}^p_{\text{eq}} = \frac{\boldsymbol{\varepsilon}^p}{||\boldsymbol{\varepsilon}^p||} : \overset{\circ}{\boldsymbol{\varepsilon}}^p = \dot{\lambda}\, \frac{\boldsymbol{\varepsilon}^p}{||\boldsymbol{\varepsilon}^p||} : \hat{\boldsymbol{M}} = \dot{\varepsilon}^p_{\text{con}}\, \frac{\boldsymbol{\varepsilon}^p}{||\boldsymbol{\varepsilon}^p||} : \hat{\boldsymbol{M}} \,. \tag{31}$$

The above relation indicates that the equivalent plastic strain and the consistent plastic strain are identical if the normalized plastic strain tensor is identical to $\hat{\boldsymbol{M}}$. We will assume that $\varepsilon^p_{\text{eq}} = \varepsilon^p_{\text{con}}$.

The Hencky strain can be additively decomposed into volumetric and isochoric parts (Xiao et al., 2004). Therefore, the equivalent plastic strain is related to the volumetric and isochoric parts of the plastic strain by the relation

$$\varepsilon^p_{\text{eq}} = ||\boldsymbol{\varepsilon}^p|| = ||\tfrac{1}{3} \varepsilon^p_v\, \boldsymbol{1} + \boldsymbol{\varepsilon}^p_{\text{iso}}|| = \sqrt{\tfrac{1}{3} \left(\varepsilon^p_v\right)^2 + \boldsymbol{\varepsilon}^p_{\text{iso}} : \boldsymbol{\varepsilon}^p_{\text{iso}}} = \sqrt{\tfrac{1}{3} \left(\varepsilon^p_v\right)^2 + ||\boldsymbol{\varepsilon}^p_{\text{iso}}||^2} \,. \tag{32}$$

---

[11] As discussed earlier, the applicability of the logarithmic rate as an objective stress rate remains questionable. Any other objective rate may be chosen instead provided the material parameters are calibrated explicitly for the rate that has been chosen. While the form used in this paper is useful for practical data fitting, a fully covariant hyperelastic-plastic formulation appears to be preferable (see, for example, Romano and Barretta (2011)) but is not pursued in this paper.

4.2.3. Non-associativity

Let us now explore the implications of non-associativity of the yield function. For simplicity, consider the situation where the plastic potential (g) is given by the ellipsoidal function in (25), i.e.,

$$g := \left(\frac{\bar{q}}{\bar{q}_s}\right)^2 + \left(\frac{\bar{p}}{\bar{p}_c}\right)^2 - 1\,. \tag{33}$$

Then, using equations (20)–(24), we have the following components of the derivatives of g in a coordinate system aligned with the reference material directions,

$$\begin{aligned} \left(\frac{\partial g}{\partial \boldsymbol{\sigma}}\right)_{11} &= \frac{2\bar{p}}{3\bar{p}_c^2} - \frac{\bar{p} - 3\sigma_{11}}{\bar{q}_s^2}\,, & \left(\frac{\partial g}{\partial \boldsymbol{\sigma}}\right)_{22} &= R\left[\frac{2\bar{p}}{3\bar{p}_c^2} - \frac{\bar{p} - 3R\sigma_{22}}{\bar{q}_s^2}\right] \\ \left(\frac{\partial g}{\partial \boldsymbol{\sigma}}\right)_{11} &= R\left[\frac{2\bar{p}}{3\bar{p}_c^2} - \frac{\bar{p} - 3R\sigma_{33}}{\bar{q}_s^2}\right]\,, & \left(\frac{\partial g}{\partial \boldsymbol{\sigma}}\right)_{23} &= 3R^2\,\frac{\sigma_{23}}{\bar{q}_s^2} \\ \left(\frac{\partial g}{\partial \boldsymbol{\sigma}}\right)_{31} &= (1+R+R^2)\,\frac{\sigma_{31}}{\bar{q}_s^2}\,, & \left(\frac{\partial g}{\partial \boldsymbol{\sigma}}\right)_{12} &= (1+R+R^2)\,\frac{\sigma_{12}}{\bar{q}_s^2} \end{aligned} \tag{34}$$

For uniaxial stress in direction 1 such that $\bar{p} = \sigma_{11}/3$, the use of the above expressions gives us

$$\overset{\circ}{\boldsymbol{\varepsilon}}{}^p = \dot{\boldsymbol{\varepsilon}}^p \equiv \frac{\dot{\lambda}}{\|\partial g/\partial \boldsymbol{\sigma}\|} \begin{bmatrix} \left(\frac{2}{9\bar{p}_c^2} + \frac{2}{\bar{q}_s^2}\right)\sigma_{11} & 0 & 0 \\ 0 & \left(\frac{2}{9\bar{p}_c^2} - \frac{1}{\bar{q}_s^2}\right)R\sigma_{11} & 0 \\ 0 & 0 & \left(\frac{2}{9\bar{p}_c^2} - \frac{1}{\bar{q}_s^2}\right)R\sigma_{11} \end{bmatrix}. \tag{35}$$

The above expression indicates that plastic strains develop in the 2–3 plane in response to an uniaxial stress in the 1 direction. While this may be true at the initial stages of deformation, experiments clearly show that out-of-plane plastic strains are close to zero during continued uniaxial compressive deformations, i.e., $\bar{q}_s^2 = 9/2\bar{p}_c^2$. It can be easily checked that this relation also gives the correct behavior for uniaxial loading in directions 2 and 3, i.e., there are no plastic strains in the directions orthogonal to the loading direction. Substitution of the value of $\bar{q}_s^2$ into the plastic potential leads to

$$g := \bar{q}^2 + \tfrac{9}{2}\left(\bar{p}^2 - \bar{p}_c^2\right)\,. \tag{36}$$

The form of the plastic potential is similar to that obtained by earlier authors such as Zhang et al. (1998, eq. 16).

If we assume that the plastic potential has the form obtained in equation (27) the components of the normal to the plastic potential surface are

$$\begin{aligned} \left(\frac{\partial g}{\partial \boldsymbol{\sigma}}\right)_{11} &= \frac{2\bar{p} - \bar{p}_c + \bar{p}_t}{3\bar{p}_c\bar{p}_t} - \frac{\bar{p} - 3\sigma_{11}}{\bar{q}_s^2}\,, & \left(\frac{\partial g}{\partial \boldsymbol{\sigma}}\right)_{22} &= R\left[\frac{2\bar{p} - \bar{p}_c + \bar{p}_t}{3\bar{p}_c\bar{p}_t} - \frac{\bar{p} - 3R\sigma_{22}}{\bar{q}_s^2}\right] \\ \left(\frac{\partial g}{\partial \boldsymbol{\sigma}}\right)_{33} &= R\left[\frac{2\bar{p} - \bar{p}_c + \bar{p}_t}{3\bar{p}_c\bar{p}_t} - \frac{\bar{p} - 3R\sigma_{33}}{\bar{q}_s^2}\right]\,, & \left(\frac{\partial g}{\partial \boldsymbol{\sigma}}\right)_{23} &= 3R^2\,\frac{\sigma_{23}}{\bar{q}_s^2} \\ \left(\frac{\partial g}{\partial \boldsymbol{\sigma}}\right)_{31} &= (1+R+R^2)\,\frac{\sigma_{31}}{\bar{q}_s^2}\,, & \left(\frac{\partial g}{\partial \boldsymbol{\sigma}}\right)_{12} &= (1+R+R^2)\,\frac{\sigma_{12}}{\bar{q}_s^2} \end{aligned} \tag{37}$$

In this case, the requirement of zero lateral plastic strain under uniaxial loads produces the constraint

$$\left[\frac{2}{9\bar{p}_c\bar{p}_t} - \frac{1}{\bar{q}_s^2}\right]\sigma_{11} = \frac{1}{3}\left(\frac{1}{\bar{p}_c} - \frac{1}{\bar{p}_t}\right)$$

If we use a yield function that is identical to g to find σ_{11}, we get the constraint

$$\frac{2}{\bar{p}_c} - \frac{2}{\bar{p}_t} - \left(\frac{\bar{q}_s}{9\bar{p}_c\bar{p}_t + \bar{q}_s^2}\right)\left(\frac{2}{\bar{p}_c\bar{p}_t} - \frac{9}{\bar{q}_s^2}\right)\left[(-\bar{p}_c + \bar{p}_t)\bar{q}_s + \sqrt{36\bar{p}_c^2\bar{p}_t^2 + (\bar{p}_c + \bar{p}_t)^2\bar{q}_s^2}\right] = 0$$

If we solve the above equation for $\bar{q}_s$, two admissible solutions are observed:

$$\bar{q}_s = 3\sqrt{\frac{\bar{p}_c\bar{p}_t(\bar{p}_c^2 + \bar{p}_t^2) \pm \sqrt{\bar{p}_c^2\bar{p}_t^2(\bar{p}_c - \bar{p}_t)^2(\bar{p}_c^2 + \bar{p}_c\bar{p}_t + \bar{p}_t^2)}}{(\bar{p}_c + \bar{p}_t)^2}}$$

These relations indicate that we can derive a number of non-associated plastic potentials that exhibit experimentally observed plastic behavior (at least for uniaxial loading) for the same yield function.

For the case where the plastic potential is identical to the yield function in equation (19), the expressions for $\partial g/\partial \boldsymbol{\sigma}$ are more involved but can be obtained in a straightforward manner from the expressions given in the previous section. For that situation, under uniaxial compression in direction 1, the requirement of zero transverse plastic strains leads to the constraint

$$\bar{q}_s^2 = \frac{81\bar{p}_c\bar{p}_t\beta_1^2\sigma_{11}}{(3\beta_1 + 2\beta\sigma_{11})\left[9\left(\beta_2 - 6\beta\bar{p}_c\bar{p}_t\right) + 6\beta_3\sigma_{11} + 8\beta\sigma_{11}^2\right]} \tag{38}$$

where

$$\beta_1 := (1-\beta)\bar{p}_c + (1+\beta)\bar{p}_t\,, \quad \beta_2 := (1+\beta)\bar{p}_t^2 - (1-\beta)\bar{p}_c^2\,, \quad \beta_3 := (1-4\beta)\bar{p}_c + (1+4\beta)\bar{p}_t\,.$$

Expressions for σ_{11} in terms of the four parameters of the yield function can be found by solving the quartic equation that results when we set all stresses except σ_{11} to zero in the yield function:

$$\frac{\sigma_{11}^2}{\bar{q}_s^2} - \left(1 - \frac{\sigma_{11}}{3\bar{p}_c}\right)\left(1 + \frac{\sigma_{11}}{3\bar{p}_t}\right)\left(1 + \frac{2\beta\sigma_{11}}{3\beta_1}\right)^2 = 0$$

If we substitute these solutions into equation (38) for $\bar{q}_s$, we get a relation between $\bar{q}_s$ and $\bar{p}_t$, $\bar{p}_c$ and β. In particular, when $\bar{p}_t = 0.17$ MPa, $\bar{p}_c = 0.22$ MPa, and $\beta = 0.4$, the admissible value of $\bar{q}_s$ is 0.41 MPa and $\sigma_{11} = \bar{q}$ is 0.43 MPa, which is smaller than the observed yield stress in uniaxial compression.

While these observations provide some insight into the relation between a yield surface and its related non-associated plastic potential, the solution of a equation (even in closed form) to determine $\bar{q}_s$ at each stage of a deformation is problematic from a computational standpoint. The trivial case where $\boldsymbol{M} = \boldsymbol{\sigma}$ satisfies the volumetric plastic strain requirement and the thermodynamic constraint provided by the Clausius-Duhem inequality, but fails to satisfy Drucker material stability constraints (Schreyer et al., 1994). It may be more convenient to follow the approach suggested by Collins and Houlsby (1997); Einav (2012) and devise a flow rule in which the direction of the plastic strain is given by

$$\boldsymbol{M} = \frac{\partial f_{\sigma\varepsilon}}{\partial \boldsymbol{\sigma}} - \frac{\partial f_{\sigma\varepsilon}}{\partial \boldsymbol{\varepsilon}^e} : \mathsf{C}^{-1} \tag{39}$$

where $f_{\sigma\varepsilon}$ is a yield function that depends both on the stress state ($\boldsymbol{\sigma}$) and the elastic strain ($\boldsymbol{\varepsilon}^e$), and C is the elastic stiffness tensor. We defer discussion of these issues to future work and suggest equation (36) as a reasonable compromise for numerical simulations.

4.2.4. Consistency condition and evolution of internal variables

The consistency condition requires that the rate of evolution of the yield surface is zero during plastic deformation, i.e.,

$$\dot{f}(\boldsymbol{\sigma}, \bar{p}_c, \bar{q}_c, \beta, R) = \frac{\partial f}{\partial \boldsymbol{\sigma}} : \mathring{\boldsymbol{\sigma}} + \frac{\partial f}{\partial \bar{p}_c}\dot{\bar{p}}_c + \frac{\partial f}{\partial \bar{q}_s}\dot{\bar{q}}_s + \frac{\partial f}{\partial \beta}\dot{\beta} + \frac{\partial f}{\partial R}\dot{R} = 0 \tag{40}$$

where $\mathring{\boldsymbol{\sigma}}$ is an appropriate objective stress rate. When the logarithmic strain ($\ln \boldsymbol{V}$) is chosen as the strain measure, a power conjugate rate is the logarithmic stress rate discussed in (Xiao et al., 1997). For simplicity, we assume that the internal variables are functions of the equivalent plastic strain, $\bar{p}_c \equiv \bar{p}_c(\varepsilon^p_{\text{eq}})$, $\bar{q}_s \equiv \bar{q}_s(\varepsilon^p_{\text{eq}})$, $\beta \equiv \beta(\varepsilon^p_{\text{eq}})$, $R \equiv R(\varepsilon^p_{\text{eq}})$. Then,

$$\dot{\bar{p}}_c = \frac{d\bar{p}_c}{d\varepsilon^p_{\text{eq}}}\dot{\varepsilon}^p_{\text{eq}} = \dot{\lambda} h_p \,,\;\; \dot{\bar{q}}_s = \frac{d\bar{q}_s}{d\varepsilon^p_{\text{eq}}}\dot{\varepsilon}^p_{\text{eq}} = \dot{\lambda} h_q \,,\;\; \dot{\beta} = \frac{d\beta}{d\varepsilon^p_{\text{eq}}}\dot{\varepsilon}^p_{\text{eq}} = \dot{\lambda} h_\beta \,,\;\; \dot{R} = \frac{dR}{d\varepsilon^p_{\text{eq}}}\dot{\varepsilon}^p_{\text{eq}} = \dot{\lambda} h_R \tag{41}$$

where h_p, h_q, h_β, h_R are "hardening" functions. Combining equations (40) and (41), we have

$$\frac{\partial f}{\partial \boldsymbol{\sigma}} : \mathring{\boldsymbol{\sigma}} + \dot{\lambda}\left(\frac{\partial f}{\partial \bar{p}_c} h_p + \frac{\partial f}{\partial \bar{q}_s} h_q + \frac{\partial f}{\partial \beta} h_\beta + \frac{\partial f}{\partial R} h_R\right) = 0\,. \tag{42}$$

We may define the ensemble hardening modulus (H) and the unit normal to the yield surface ($\hat{\boldsymbol{N}}$) as (Brannon, 2007)

$$H := -\left(\frac{\partial f}{\partial \bar{p}_c} h_p + \frac{\partial f}{\partial \bar{q}_s} h_q + \frac{\partial f}{\partial \beta} h_\beta + \frac{\partial f}{\partial R} h_R\right) \Big/ \left\| \frac{\partial f}{\partial \boldsymbol{\sigma}} \right\| \quad \text{and} \quad \hat{\boldsymbol{N}} := \frac{\boldsymbol{N}}{\|\boldsymbol{N}\|} = \frac{\partial f}{\partial \boldsymbol{\sigma}} \Big/ \left\| \frac{\partial f}{\partial \boldsymbol{\sigma}} \right\| \tag{43}$$

to get the consistency condition and an alternative form of the flow rule:

$$\hat{\boldsymbol{N}} : \mathring{\boldsymbol{\sigma}} = \dot{\lambda} H \quad \text{and} \quad \mathring{\boldsymbol{\varepsilon}}^p = \frac{1}{H}\hat{\boldsymbol{N}}(\hat{\boldsymbol{N}} : \mathring{\boldsymbol{\sigma}})\,. \tag{44}$$

This alternative form of the flow rule is similar to that derived by Bruhns (2009) from a dissipation inequality. The derivatives of f with respect to the internal variables are

$$\begin{aligned}
\frac{\partial f}{\partial \bar{p}_c} &= -\frac{\bar{p}(\bar{p} + \bar{p}_t)}{\bar{p}_c^2\, \bar{p}_t\, \beta_1^3}(\beta_1 + 2\beta\bar{p}) \times \\
&\qquad \Big[(1-\beta)\left[(1-5\beta)\bar{p}_c + 6\beta\bar{p}\right]\bar{p}_c + (1+\beta)\left[\beta_1 + (1-\beta)\bar{p}_c + 2\beta\bar{p}\right]\bar{p}_t\Big] \\
\frac{\partial f}{\partial \bar{q}_s} &= -\frac{2\bar{q}^2}{\bar{q}_s^3} \\
\frac{\partial f}{\partial \beta} &= \frac{4\bar{p}(\bar{p} + \bar{p}_t)}{\bar{p}_c\, \bar{p}_t\, \beta_1^3}(\beta_1 + 2\beta\bar{p})(\bar{p} - \bar{p}_c)(\bar{p}_c + \bar{p}_t) \\
\frac{\partial f}{\partial R} &= \frac{\partial f}{\partial \bar{p}}\frac{\partial \bar{p}}{\partial R} + \frac{\partial f}{\partial \bar{q}}\frac{\partial \bar{q}}{\partial R} = \frac{1}{3}\frac{\partial f}{\partial \bar{p}}(\sigma_{22} + \sigma_{33}) + \\
&\qquad \frac{1}{\bar{q}_s^2}\Big[(1+2R)\left(\sigma_{12}^2 + \sigma_{31}^2\right) + 6R\sigma_{23}^2 + 2R(\sigma_{22} - \sigma_{33})^2 + 2R\sigma_{22}\sigma_{33} - \sigma_{11}(\sigma_{22} + \sigma_{33})\Big]
\end{aligned} \tag{45}$$

The simple shear tests described in Section 3.6 can be used to calibrate the quantity h_q. The calibration is performed by sampling plots of $\bar{q}$ versus γ^p_{eq} (the Hencky equivalent shear strain) at equal intervals and fitting tangents to the curves at these sampling points. The resulting tangent (h_q) values are observed to be approximately linear functions of γ^p_{eq} (as shown in Figure 18) and can be described by a hardening rule of the form

$$h_q = h_{q0}\exp(h_{q1}\gamma^p_{\text{eq}}) \quad \Longrightarrow \quad \bar{q}_s = \bar{q}_{s0} + \frac{h_{q0}}{h_{q1}}\left[\exp(h_{q1}\gamma^p_{\text{eq}}) - 1\right] \tag{46}$$

where $\bar{q}_{s0}$ is the value of $\bar{q}$ at initial yield, h_{q0} is the initial hardening modulus, and h_{q1} is the slope of the hardening modulus curve. Note that quadratic evolution rules for $\bar{q}$ as suggested by Maier et al. (2003) lead to unstable softening at moderate to large uniaxial compressive strains and are not suitable for computational modeling. While

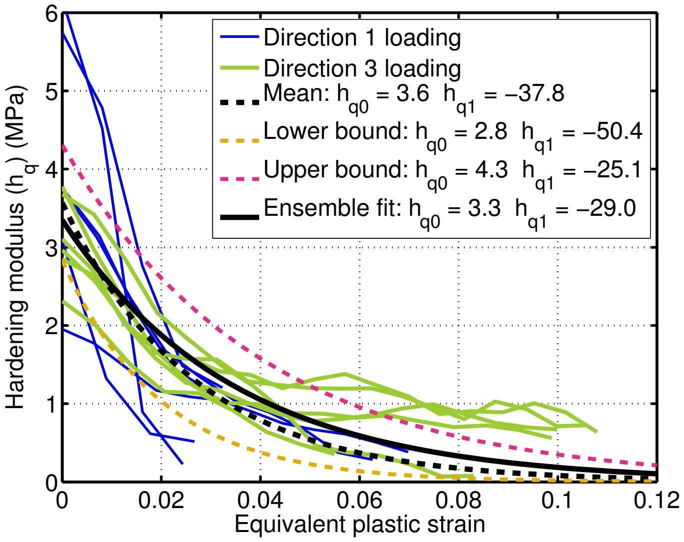

Figure 18: Hardening modulus (h_q) as a function of the equivalent Hencky plastic shear strain for PU foam samples tested in shear. The mean is the average of separate fits to the individual curves. The ensemble mean is a least squares fit of all the data. The upper and lower bounds represent 90% confidence intervals around the mean assuming a t-distribution.

the initial hardening modulus lies largely within a limited range between 2 to 4 MPa, the initial slopes of the hardening curves range from -17 to -265 MPa. An average response for the foam is therefore difficult to determine and two possibilities are shown in Figure 18. The ensemble fit values of $h_{q0} = 3.3$ MPa and $h_{q1} =$ -29 have been found to approximate the shear stress-strain behavior of the foam reasonably well.

Calibration of the hardening moduli h_p and h_β is more involved. One possibility is to use test data from hydrostatic compression and uniaxial compression in the rise direction. In those situations, if p_f is the pressure in the hydrostatic compression test and σ_{11} is the compressive stress in the uniaxial compression test, the yield condition reduces to

$$\begin{aligned} g = C_1\,\bar{p}_c\left[(1-\beta)\bar{p}_c + (1+\beta)\bar{p}_t\right]^2 - \\ (\bar{p}_c - C_2)\,(\bar{p}_t + C_2)\left[(1-\beta)\bar{p}_c + (1+\beta)\bar{p}_t + 2\beta C_2\right]^2 = 0 \end{aligned} \tag{47}$$

where the quantities C_1 and C_2 are functions of the applied stress. The above equation is quadratic in β and cubic in $\bar{p}_c$. In principle, we could solve a quadratic equation to get an expression for β in terms of p_c and the other known quantities. Alternatively we could solve a cubic equation for $\bar{p}_c$.

However, both these approaches have been found to be unsuitable for practical calibration purposes. Instead, based on the $\bar{p}$-$\bar{q}$ plots discussed earlier, we assume that β increases from 0 to a saturation value of 0.8. The resulting models for β and h_β are

$$\beta = \beta_s\left[\tanh\left(\beta_{t1}\,\varepsilon^p_{\text{eq}} - \beta_{t2}\right) + \tanh(\beta_{t2})\right] \quad \text{and} \quad h_\beta = \beta_s\,\beta_{t1}\,\text{sech}^2\left(\beta_{t1}\,\varepsilon^p_{\text{eq}} - \beta_{t2}\right) \tag{48}$$

where $\beta_s = 0.4$ is half the saturation value of β, and $\beta_{t1} = \beta_{t2} = 1.5$ are parameters that control the rate of increase of beta with increasing plastic strain. A plot of the variation of β with plastic strain is shown in Figure 19.

For hydrostatic tests $\bar{p} = 1/3(1+2R)p_f$ and $\bar{q} = (R-1)p_f$. To calibrate an adequate hardening model for p_c, we need tests during which $\bar{q} = 0$ for logarithmic strains up to ∼1.5. In the absence of specialized equipment, the pressure in the fluid could not be controlled adequately for true compressive strains larger than approximately 0.3. Because we were unable to maintain the required stress state in our experiments, we projected values of $\bar{p}$ from a standard hydrostatic test on to the $\bar{p}$ axis (where $\bar{q} = 0$) and used these projected values to fit the model. This approximation is reasonable given the flattened shape of the piriform yield surface as the curve approaches the $\bar{p}$ axis.

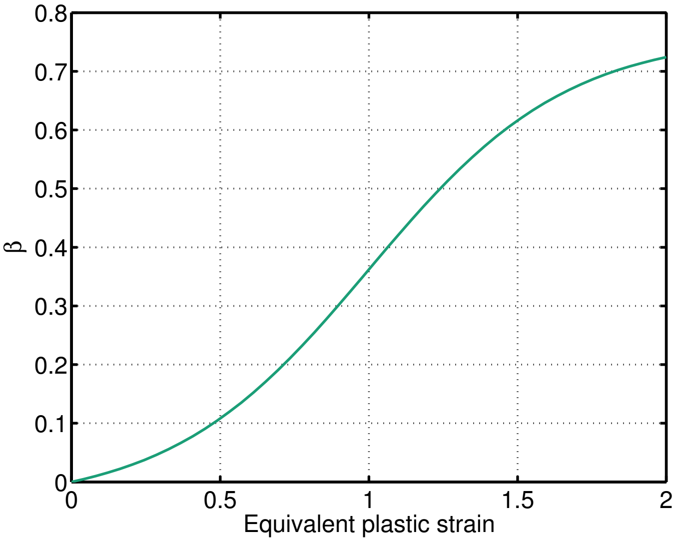

Figure 19: Evolution of the shape parameter β as a function of plastic strain for PU foam. The model is given by equation (48).

Examination of the stress-strain curve for hydrostatic compression of the PU foam indicates a decrease in the hardening modulus with increasing strain which is contrary to the behavior observed in uniaxial compression. This is partly because of the limited range of strain (maximum equivalent plastic strain ~0.8) for the test. To counter this lack of data, we fitted hardening models to the uniaxial compression data and then scaled the models to obtain a the hydrostatic compression test.

Figure 20 shows a plot of the hardening modulus $d\bar{p}/d\varepsilon^p_{\text{eq}}$ for the uniaxial compression tests as a function of the equivalent plastic strain. The shape anisotropy factor (R) used in the calculation of $\bar{p}$ for the tests in directions 2 and 3 is given by equation (11) with $R_0 = 0.4$ and $R_1 = 1.0$. As can be observed from the figure, the use of this variable value of R leads to the overlap of hardening curves in the three principal material directions. The stress-strain curves for uniaxial compression indicate that the initial hardening modulus is low and increases with plastic strain. However, at large plastic strains corresponding to full compression the hardening modulus is expected to approach the elastic modulus of the PU material. We attempt to model this behavior with a sigmoidal curve of the form

$$\frac{d\bar{p}}{d\varepsilon^p_{\text{eq}}} = h_1\left[1 + \tanh(h_2\,\varepsilon^p_{\text{eq}} - h_3)\right] \tag{49}$$

where h_1, h_2, h_3 are constants. The ensemble least squares fit shown in Figure 20 generated values of $h_1 = 0.6$ MPa, $h_2 = 1.3$, and $h_3 = 2.2$. Integration of the above equation leads to

$$\bar{p} = \bar{p}_0 + h_1\,\varepsilon^p_{\text{eq}} + \frac{h_1}{h_2}\left[\ln\left[\cosh(h_2\,\varepsilon^p_{\text{eq}} - h_3)\right] - \ln\left[\cosh(h_3)\right]\right] \tag{50}$$

where $\bar{p}_0$ is the value of $\bar{p}$ at initial yield. If we assume that $\bar{p}_c = \bar{p}_t = 0.18$ MPa at $\varepsilon^0_{\text{eq}} = 0$, the value of $\bar{p}_0 = \sigma_{11}/3 = R\sigma_{22}/3$ is 0.105 MPa.

At this stage we assume that $\bar{p}_t = 0.18$ MPa and that $\bar{q}_s$, β, and $\bar{q} = 3\bar{p}$ are given by the models in (46), (48), and (50), respectively. If we substitute these into the yield function we get a cubic equation in $\bar{p}_c$ and $\varepsilon^p_{\text{eq}}$ which can be solved numerically for $\bar{p}_c$ at various values of $\varepsilon^p_{\text{eq}}$. The resulting values of $\bar{p}_c$ plotted as a function of the equivalent plastic strain are shown as points in Figure 21. We assume that $\bar{p}_c(\varepsilon^p_{\text{eq}})$ has the same form as equation (49), i.e.,

$$\bar{p}_c = \bar{p}_{c0} + h_{p1}\,\varepsilon^p_{\text{eq}} + \frac{h_{p1}}{h_{p2}}\left[\ln\left[\cosh(h_{p2}\,\varepsilon^p_{\text{eq}} - h_{p3})\right] - \ln\left[\cosh(h_{p3})\right]\right]. \tag{51}$$

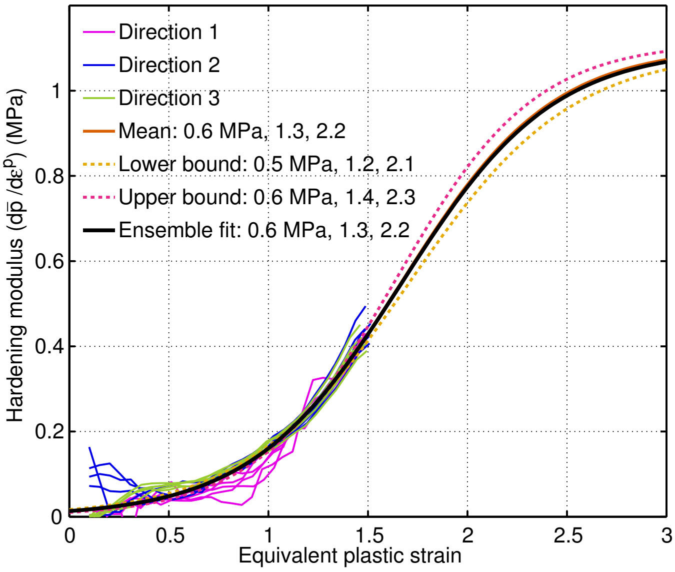

Figure 20: Hardening modulus ($d\bar{p}/d\varepsilon^p_{\text{eq}}$) for uniaxial compression tests as a function of the equivalent Hencky plastic strain for PU foam samples. The mean is the average of separate fits to each individual curve. The ensemble fit is a least squares fit to all the data. The upper and lower bounds represent 95% confidence intervals around the mean assuming a t-distribution. The fitted parameters are listed in the sequence (h_1 MPa, h_2, h_3).

A least squares fit to the $\bar{p}_c$ points gives us the model parameters $\bar{p}_{c0} = 0.18$ MPa, $h_{p1} = 5.2$ MPa, $h_{p2} = 1.2$, and $h_{p3} = 3.0$. The fitted curve and the hardening plot from the hydrostatic test are also shown in Figure 21.

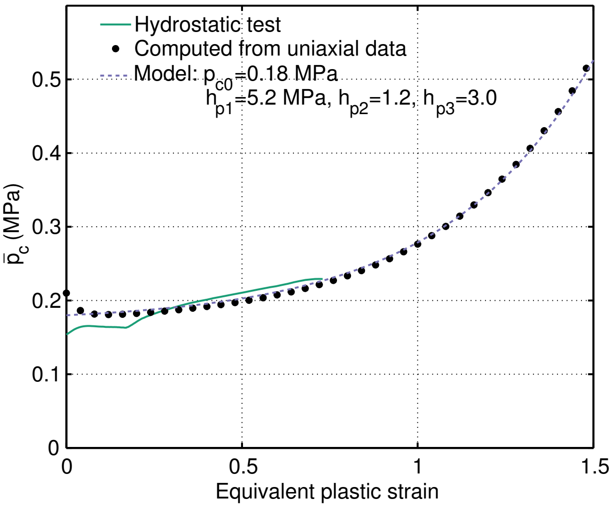

Figure 21: Scaled mean stress $\bar{p}_c$ as a function of plastic strain from hydrostatic compression test on PU foam sample. The model is given by equation (51).

The value of $\bar{p}_c$ (shown as filled circles in the figure) at $\varepsilon^p_{\text{eq}} = 0$ is ∼0.2 MPa and initially decreases with increase in plastic strain. This behavior is similar to that observed in uniaxial compression in direction 1 and points at the possibility that if we start with a fit to the appropriate hydrostatic test curve and compute β, we may be able to reproduce the initial drop in yield stress observed in uniaxial compression. More importantly, from an empirical standpoint, the drop indicates that the value of β at zero plastic strain cannot be zero and probably has a negative value. Another possibility is that the assumption that $\bar{p}_c = \bar{p}_t$ at $\varepsilon^p_{\text{eq}} = 0$ is incorrect. Exploration of the issue has indicated that a better fit to the data is obtained when $\bar{p}_{c0} = 0.125$ MPa and $\bar{p}_t = 0.18$ MPa and these are the values that have been used in the model predictions shown in Section 4.3.

4.3. *Model summary and predictions*

The elastic behavior of the foam can be modeled using a hypoelastic model of the form

$$\overset{\circ}{\boldsymbol{\sigma}} = \mathsf{C}(\boldsymbol{\varepsilon}) : (\overset{\circ}{\boldsymbol{\varepsilon}} - \overset{\circ}{\boldsymbol{\varepsilon}}{}^p)$$

where a logarithmic rate is assumed and $\boldsymbol{\varepsilon}^p$ is the plastic part of Hencky logarithmic strain ($\boldsymbol{\varepsilon}$). The flow rule is not associated with the yield surface and is assumed to be of the form

$$\overset{\circ}{\boldsymbol{\varepsilon}}{}^p = \dot{\lambda} \frac{\partial g}{\partial \boldsymbol{\sigma}} \quad \text{where} \quad g = \bar{q}^2 + \tfrac{9}{2}\left(\bar{p}^2 - \bar{p}_c^2\right)$$

with

$$\begin{aligned} \bar{p} &= \tfrac{1}{3}(\sigma_{11} + R\sigma_{22} + R\sigma_{33}), \\ \bar{q}^2 &= \tfrac{1}{2}\left[(\sigma_{11} - R\sigma_{22})^2 + R^2(\sigma_{22} - \sigma_{33})^2 + (R\sigma_{33} - \sigma_{11})^2\right] + \\ &\qquad 3R^2\sigma_{23}^2 + (1 + R + R^2)(\sigma_{31}^2 + \sigma_{12}^2). \end{aligned}$$

The piriform yield surface is expressed as

$$f := \left(\frac{\bar{q}}{\bar{q}_s}\right)^2 - \left(1 - \frac{\bar{p}}{\bar{p}_c}\right)\left(1 + \frac{\bar{p}}{\bar{p}_t}\right)\left[1 + \frac{2\beta\,\bar{p}}{(1-\beta)\,\bar{p}_c + (1+\beta)\,\bar{p}_t}\right]^2 = 0.$$

The models for the evolution of the internal variables are

$$\begin{aligned} \bar{q}_s &= \bar{q}_{s0} + \frac{h_{q0}}{h_{q1}}\left[\exp(h_{q1}\,\gamma^p_{\text{eq}}) - 1\right] \\ \bar{p}_c &= \bar{p}_{c0} + h_{p1}\,\varepsilon^p_{\text{eq}} + \frac{h_{p1}}{h_{p2}}\left[\ln\left[\cosh(h_{p2}\,\varepsilon^p_{\text{eq}} - h_{p3})\right] - \ln\left[\cosh(h_{p3})\right]\right] \\ \beta &= \beta_s\left[\tanh\left(\beta_{t1}\,\varepsilon^p_{\text{eq}} - \beta_{t2}\right) + \tanh(\beta_{t2})\right] \\ R &= 1.0 + R_0\,\exp(-R_1\,\varepsilon^p_{\text{eq}}) \end{aligned}$$

where $\varepsilon^p_{\text{eq}} = \sqrt{\boldsymbol{\varepsilon}^p : \boldsymbol{\varepsilon}^p}$ and $\gamma^p_{\text{eq}} = \sqrt{\boldsymbol{\varepsilon}^p_{\text{iso}} : \boldsymbol{\varepsilon}^p_{\text{iso}}}$.

In this paper we use the mean values of model parameters to compare our model with experimental data and relegate the detailed examination of material variability effects to future work. For the elasticity model we use initial values of

$$E_{11} = 16 \text{ MPa}\,, \;\; E_{22} = E_{33} = 4.9 \text{ MPa}\,, \;\; G_{12} = 6.0 \text{ MPa}\,, \;\; \nu_{12} = \nu_{13} = \nu_{23} = 0.3\,.$$

The Poisson's ratios are modified according to equations (2) as deformation proceeds. The internal variable model parameters are

$$\begin{aligned} &\bar{q}_{s0} = 0.4 \text{ MPa}\,, \;\; h_{q0} = 3.3 \text{ MPa}\,, \;\; h_{q1} = -29 \\ &\bar{p}_{c0} = 0.12 \text{ MPa}\,, \;\; h_{p1} = 5.2 \text{ MPa}\,, \;\; h_{p2} = 1.2\,, \;\; h_{p3} = 3.0 \\ &\beta_s = 0.4\,, \;\; \beta_{t1} = 1.5\,, \;\; \beta_{t2} = 1.5 \\ &R_0 = 0.4\,, \;\; R_1 = 1.0\,. \end{aligned}$$

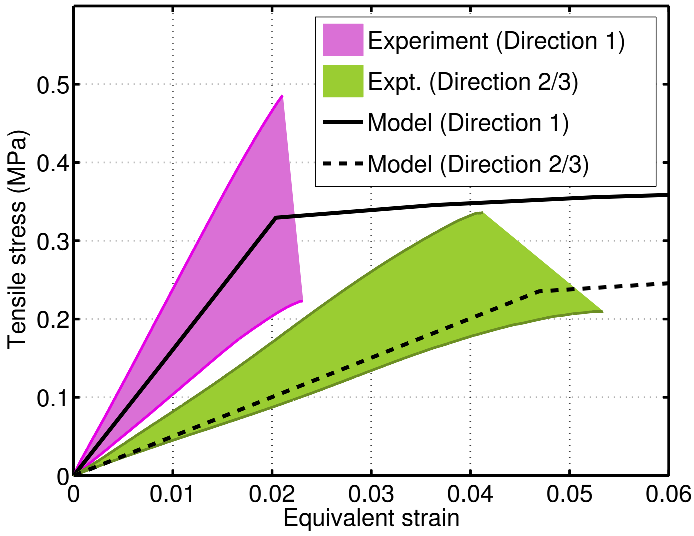

Figure 22: Uniaxial tension: comparison of model prediction and experimental data.

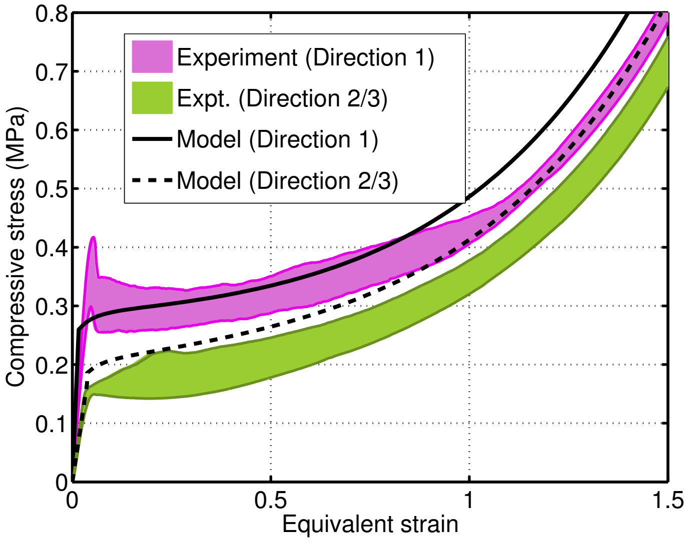

Figure 23: Uniaxial compression: comparison of model prediction and experimental data.

A plot of the mean uniaxial tension stress-strain behavior predicted by the model is compared with experimental data in Figure 22. A damage model with a tensile cut-off is needed for the post yield tensile behavior to be modeled correctly.

Figure 23 shows the stress-strain behavior for uniaxial compression. The model predicts a higher initial modulus than that exhibited by the data leading to a overestimation of the yield stress at large strains. The model also predicts a larger value of the yield stress in the 2 and 3 directions, indicating that the use of an identical shape anisotropy ratio (R) in both tension and compression may not be adequate.

The stress-strain behavior predicted by the model for hydrostatic compression is compared with the experimental data in Figure 24. A smaller effective bulk modulus is observed in the experiment than that predicted by the model but may be related to the large variability observed in the PU foam.

Triaxial compression data for two confining pressures and axial loading in direction 3 are compared with model

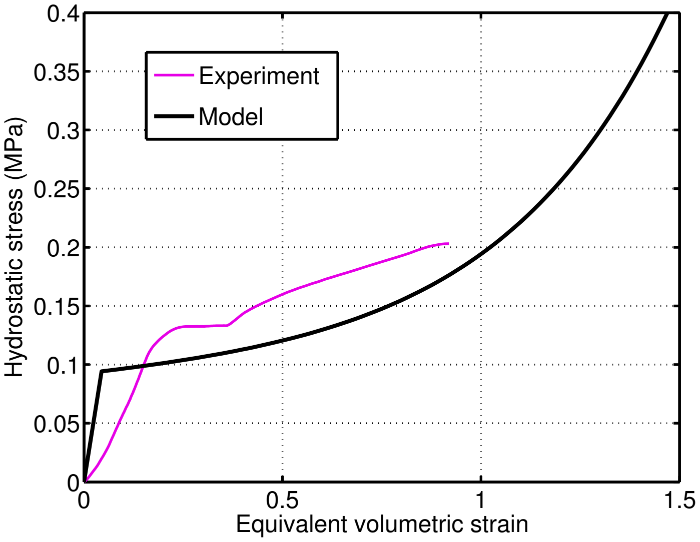

Figure 24: Hydrostatic compression: comparison of model prediction and experimental data.

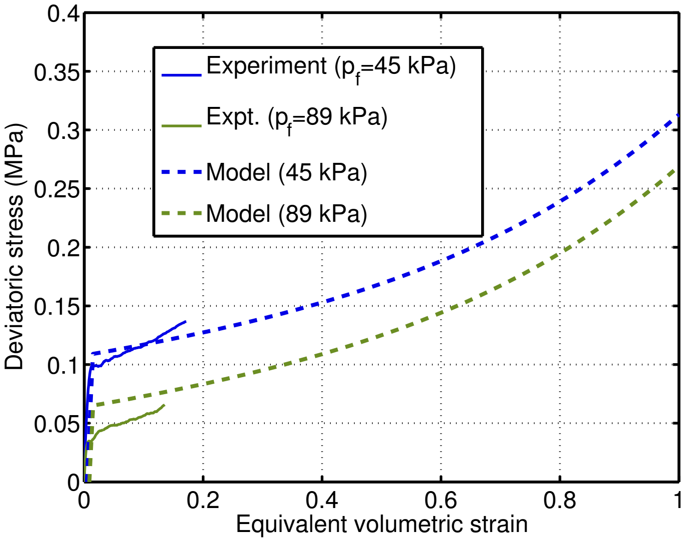

Figure 25: Triaxial compression: comparison of model prediction and experimental data. The deviatoric stress in the ordinate is defined as $\sigma_3 - p_f$ where σ_3 is the axial stress and p_f is the confining pressure.

predictions in Figure 25. The model predictions are in reasonably good agreement with experiment. However, in this case the initial hardening modulus appears to be underestimated by the model.

The mean response of the foam in pure shear is also predicted adequately by the model as shown in Figure 26. In this case too, as was observed for the tension tests, a damage and softening model is needed if the post failure behavior is to be predicted. We have found that the expedient approach of degrading $\bar{p}_t$ and $\bar{q}_s$ with increasing strain is not adequate. Further study is required into thermodynamically consistent damage models for the foam.

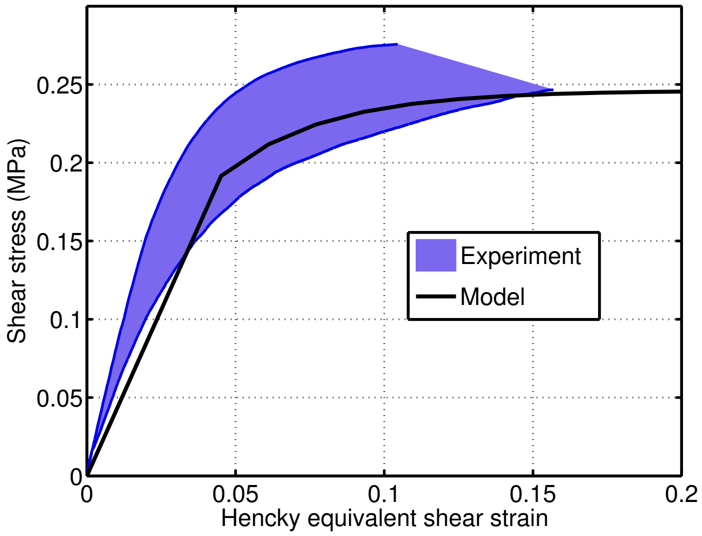

Figure 26: Shear: comparison of model prediction and experimental data.

5. Conclusions

We have presented the detailed characterization of an anisotropic low density polyurethane foam and developed a novel piriform yield surface and hardening models to predict the elastic-plastic behavior of the foam. The foam is strongly anisotropic with the largest elastic moduli and yield strengths in the rise direction. While the behavior of the foam in the transverse directions perpendicular to the rise direction is not exactly isotropic, the assumption of transverse isotropy can be used to simplify predictive simulations. Tension, compression, and fracture toughness tests indicate that the shape anisotropy ratio of the foam is approximately 1.4 at low strains. The anisotropy ratio decreases with increasing compressive strain. The strain at rupture for uniaxial tension in the rise direction is approximately half that for tension in the transverse directions. Similar behavior is observed for the strain at initial yield for uniaxial compression, i.e., the yield strain in the rise direction is significantly smaller than that in the transverse directions. Triaxial compression and simple shear tests also indicate direction dependence.

The material exhibits a significant amount of variability even though the density variation between samples is small. In uniaxial tension tests the elastic modulus is found to vary between $\sim 7-30\%$ as do the stress and strain at rupture. A large range of variation ($\sim 4-20\%$) is also observed in uniaxial compression tests. Interestingly, the initial hardening modulus for uniaxial compression in transverse direction 2 is found to be an order of magnitude higher than that in the two orthogonal directions. This behavior has been observed in other studies on PU foams but is not well explained at this stage. We speculate that the microstructure of cell walls in the plane perpendicular to direction 2 may inhibit buckling and cause the apparent initial hardening. Simple shear tests on the foam indicate an initial elastic-plastic phase followed by brittle failure. The variability in shear yield strength and shear stress at rupture is $\sim$10% while the strain at rupture can vary up to $\sim$40% and is strongly dependent on loading direction. The range of variability in the fracture toughness of the foam is $\sim 12-25\%$.

Examination of the experimental data in mean stress-deviatoric stress space indicates a closed yield surface that flattens with progressive compressive deformation. A new anisotropic yield surface has been developed that uses the shape anisotropy ratio and a piriform curve to model the observed data. The new yield surface and the associated hardening models describe the mean response of the foam reasonably well. The elasticity and plasticity models have been described in terms of Eulerian logarithmic strains and logarithmic rates. A non-associated flow rule is suggested on the basis of the observation that the plastic Poisson's ratio of the foam is close to zero. While the piriform yield surface is superior to Drucker-Prager models with caps, it is worth pointing out that the yield function is not convex in the entire stress space and has a small region with a local maximum in the domain beyond the triaxial tension yield point. Nevertheless, our models possess excellent smoothness characteristics and can model most of the range of behaviors expected during the deformation of foam-filled sections. When the parameter β is zero and shape anisotropy ratio R is one, the piriform model reduces to an ellipsoidal model similar to those used for isotropic foams and soils. The models developed in this paper can also be readily implemented into numerical codes and used to simulate not only foams but also geomaterials. Structure-property relationships can be used to scale the model parameters for application to foams of different densities and microstructures.

Acknowledgement

This research was funded by the Materials Accelerator at the University of Auckland, New Zealand. We appreciate the support provided by Dr. Choung Nguyen, Dr. Mark Exley, and Dr. Xun Xu from the University of Auckland and Dr. Diana Siew from Industrial Research Limited, Auckland, New Zealand. The facilities and testing equipment were provided by the Centre for Advanced Composite Materials of the University of Auckland and by Industrial Research Limited. We are also thankful to Prof. Rebecca Brannon for reviewing an early draft of the paper and suggesting several improvements.

References

Acharya, A., Shawki, T.G., 1996. The Clausius-Duhem inequality and the structure of rate-independent plasticity. International Journal of Plasticity 12, 229–238.

Alkhader, M., Vural, M., 2010. A plasticity model for pressure-dependent anisotropic cellular solids. International Journal of Plasticity 26, 1591–1605.

Arghavani, J., Auricchio, F., Naghdabadi, R., 2011. A finite strain kinematic hardening constitutive model based on Hencky strain: general framework, solution algorithm and application to shape memory alloys. International Journal of Plasticity 27, 940–961.

ASTM-C273/C273M-07a, 2010. Standard test method for shear properties of sandwich core materials, in: ASTM Standard C273/C273M. ASTM International, West Conshohocken, PA.

ASTM-C297-04, 2010. Standard test method for flatwise tensile strength of sandwich constructions, in: ASTM Standard C297/C297M-04. ASTM International, West Conshohocken, PA.

ASTM-D1621-10, 2010. Standard test method for compressive properties of rigid cellular plastics, in: ASTM Standard D1621. ASTM International, West Conshohocken, PA.

ASTM-D2850-03a, 2007. Standard test method for unconsolidated-undrained triaxial compression test for cohesive soils, in: ASTM Standard D2850-03a. ASTM International, West Conshohocken, PA.

ASTM-D3039-08, 2008. Standard test method for tensile properties of polymer matrix composite materials, in: ASTM Standard D3039/D3039M. ASTM International, West Conshohocken, PA.

ASTM-D4767-11, 2011. Standard test method for consolidated undrained triaxial compression test for cohesive soils, in: ASTM Standard D4767-11. ASTM International, West Conshohocken, PA.

ASTM-D5045-99, 2007. Standard test methods for plane-strain fracture toughness and strain energy release rate of plastic materials, in: ASTM Standard D5045-99. ASTM International, West Conshohocken, PA.

ASTM-D638-10, 2010. Standard test method for tensile properties of plastics, in: ASTM Standard D638. ASTM International, West Conshohocken, PA.

Bertram, A., Krawietz, A., 2012. On the introduction of thermoplasticity. Acta Mechanica , 1–12.

Bishop, A.W., Henkel, D.J., 1962. The measurement of soil properties in the triaxial test. E. Arnold. London (1982 printing).

Bouix, R., Viot, P., Lataillade, J.L., 2009. Polypropylene foam behaviour under dynamic loadings: Strain rate, density and microstructure effects. International Journal of Impact Engineering 36, 329–342.

Brannon, R., 2007. Elements of phenomenological plasticity: Geometrical insight, computational algorithms, and topics in shock physics. ShockWave Science and Technology Reference Library , 225–274.

Bruhns, O.T., 2009. Eulerian elastoplasticity: Basic issues and recent results. Theoretical and Applied Mechanics 36, 167–205.

Bruhns, O.T., Xiao, H., Meyers, A., 1999. Self-consistent eulerian rate type elasto-plasticity models based upon the logarithmic stress rate. International Journal of Plasticity 15, 479–520.

Burteau, A., N'Guyen, F., Bartout, J.D., Forest, S., Bienvenu, Y., Saberi, S., Naumann, D., et al., 2012. Impact of material processing and deformation on cell morphology and mechanical behavior of polyurethane and nickel foams. International Journal of Solids and Structures 49, 2714–2732.

Chandler, H.W., Sands, C.M., 2010. Including friction in the mathematics of classical plasticity. International journal for numerical and analytical methods in geomechanics 34, 53–72.

Choi, J.B., Lakes, R.S., 1992. Non-linear properties of polymer cellular materials with a negative Poisson's ratio. Journal of Materials Science 27, 4678–4684.

Collins, I.F., Houlsby, G.T., 1997. Application of thermomechanical principles to the modelling of geotechnical materials. Proceedings of the Royal Society of London. Series A: Mathematical, Physical and Engineering Sciences 453, 1975–2001.

Combaz, E., Bacciarini, C., Charvet, R., Dufour, W., Dauphin, F., Mortensen, A., 2010. Yield surface of polyurethane and aluminium replicated foam. Acta Materialia 58, 5168–5183.

Criscione, J.C., Humphrey, J.D., Douglas, A.S., Hunter, W.C., 2000. An invariant basis for natural strain which yields orthogonal stress response terms in isotropic hyperelasticity. Journal of the Mechanics and Physics of Solids 48, 2445–2465.

Criscione, J.C., S Douglas, A., Hunter, W.C., 2001. Physically based strain invariant set for materials exhibiting transversely isotropic behavior. Journal of the Mechanics and Physics of Solids 49, 871–897.

Daniel, I.M., Cho, J.M., 2011. Characterization of anisotropic polymeric foam under static and dynamic loading. Experimental Mechanics 51, 1395–1403.

Daniel, I.M., Gdoutos, E.E., 2010. Failure modes of composite sandwich beams, in: Major Accomplishments in Composite Materials and Sandwich Structures. Springer, pp. 197–227.

Deshpande, V.S., Fleck, N.A., 2000. Isotropic constitutive models for metallic foams. Journal of the Mechanics and Physics of Solids 48, 1253–1283.

Deshpande, V.S., Fleck, N.A., 2001. Multi-axial yield behaviour of polymer foams. Acta Materialia 49, 1859–1866.

Einav, I., 2012. The unification of hypo-plastic and elasto-plastic theories. International Journal of Solids and Structures 49, 1305–1315.

Everitt, S.L., Harlen, O.G., Wilson, H.J., 2006. Competition and interaction of polydisperse bubbles in polymer foams. Journal of non-newtonian fluid mechanics 137, 60–71.

Exley, M., Nguyen, C., Clifton, C., 2010a. Compression test of lipped C steel sections: different foam densities. Unpublished report.

Exley, M., Nguyen, C., Clifton, C., 2010b. Compression test of lipped C steel sections: different steel gauges, foam with a half-pipe void, and different surface pretreatments. Unpublished report.

Exley, M., Nguyen, C., Clifton, C., 2011a. Bending test of lipped C steel sections: flange down orientation. Unpublished report.

Exley, M., Nguyen, C., Clifton, C., 2011b. Bending test of lipped C steel sections: web down orientation. Unpublished report.

Fowlkes, C., 1974. Fracture toughness tests of a rigid polyurethane foam. International Journal of Fracture 10, 99–108.

Gibson, L.J., 2000. Mechanical behavior of metallic foams. Annual Review of Materials Science 30, 191–227.

Gibson, L.J., Ashby, M.F., 1982. The mechanics of three-dimensional cellular materials. Proceedings of the Royal Society of London. A. Mathematical and Physical Sciences 382, 43–59.

Gibson, L.J., Ashby, M.F., 1999. Cellular solids: structure and properties. Cambridge University Press.

Gibson, L.J., Ashby, M.F., Schajer, G.S., Robertson, C.I., 1982. The mechanics of two-dimensional cellular materials. Proceedings of the Royal Society of London. A. Mathematical and Physical Sciences 382, 25–42.

Gibson, L.J., Ashby, M.F., Zhang, J., Triantafillou, T.C., 1989. Failure surfaces for cellular materials under multiaxial loads I. Modelling. International Journal of Mechanical Sciences 31, 635–663.

Hanssen, A.G., Hopperstad, O.S., Langseth, M., Ilstad, H., 2002. Validation of constitutive models applicable to aluminium foams. International Journal of Mechanical Sciences 44, 359–406.

Head, K.H., 1980. Effective stress tests, in: Manual of soil laboratory testing: Volume 3. Pentech Press, London, pp. 1980–1986.

Houlsby, G.T., 2003. Some mathematics for the constitutive modelling of soils. Advanced Mathematical and Computational Geomechanics , 35.

Huber, A.T., Gibson, L.J., 1988. Anisotropy of foams. Journal of Materials Science 23, 3031–3040.

ISO-844, 2001. Rigid cellular plastics - determination of compression properties, in: ISO 844-2001 (E). International Standards Organization.

Jin, H., Lu, W., Hong, S., Connelly, K., 2007a. Fracture behavior of polyurethane foams, in: Proceedings of the 2007 SEM Annual Conference and Exposition on Experimental and Applied Mechanics, Springfield, Massachusetts.

Jin, H., Lu, W., Scheffel, S., Hinnerichs, T., Neilsen, M., 2007b. Full-field characterization of mechanical behavior of polyurethane foams. International Journal of Solids and Structures 44, 6930–6944.

Kabir, M.E., Saha, M.C., Jeelani, S., 2006. Tensile and fracture behavior of polymer foams. Materials Science and Engineering: A 429, 225–235.

Kraus, B., 2012. Characterizing polyurethane foam behaviour and interfacial failure of metal-polymer interface on composite beams. Master's thesis. Department of Mechanical Engineering, University of Auckland, Auckland, NZ.

Ling, H.I., Yue, D., Kaliakin, V.N., Themelis, N.J., 2002. Anisotropic elastoplastic bounding surface model for cohesive soils. Journal of engineering mechanics 128, 748–758.

Maier, M., Huber, U., Mkrtchyan, L., Fremgen, C.M., 2003. Recent improvements in experimental investigation and parameter fitting for cellular materials subjected to crash loads. Composites Science and Technology 63, 2007–2012.

Maiti, S.K., Gibson, L.J., Ashby, M.F., 1984. Deformation and energy absorption diagrams for cellular solids. Acta Metallurgica 32, 1963–1975.

McElwain, D., Roberts, A., Wilkins, A., 2006. Yield criterion of porous materials subjected to complex stress states. Acta materialia 54, 1995–2002.

McIntyre, A., Anderton, G.E., 1979. Fracture properties of a rigid polyurethane foam over a range of densities. Polymer 20, 247–253.

Mohr, D., 2005. Mechanism-based multi-surface plasticity model for ideal truss lattice materials. International Journal of Solids and Structures 42, 3235–3260.

Moore, B., Jaglinski, T., Stone, D.S., Lakes, R.S., 2006. Negative incremental bulk modulus in foams. Philosophical Magazine Letters 86, 651–659.

Niknejad, A., Elahi, S.A., Liaghat, G.H., 2012. Experimental investigation on the lateral compression in the foam-filled circular tubes. Materials & Design 36, 24–34.

Onaka, S., 2012. Comment on âĂIJa comparison of the von Mises and Hencky equivalent strains for use in simple shear experimentsâĂİ. Philosophical Magazine 92, 2264–2271.

Pivonka, P., Willam, K., 2003. The effect of the third invariant in computational plasticity. Engineering Computations 20, 741–753.

Ranganathan, S.I., Ostoja-Starzewski, M., 2008. Universal elastic anisotropy index. Physical Review Letters 101, 55504.

Reddy, T.Y., Wall, R.J., 1988. Axial compression of foam-filled thin-walled circular tubes. International Journal of Impact Engineering 7, 151–166.

Reid, S.R., Reddy, T.Y., Gray, M.D., 1986. Static and dynamic axial crushing of foam-filled sheet metal tubes. International Journal of Mechanical Sciences 28, 295–322.

Roberts, A.P., Garboczi, E.J., 2002. Elastic properties of model random three-dimensional open-cell solids. Journal of the Mechanics and Physics of Solids 50, 33–55.

Rodríguez-Pérez, M.A., Campo-Arnáiz, R.A., Aroca, R.F., De Saja, J.A., 2005. Characterisation of the matrix polymer morphology of polyolefins foams by raman spectroscopy. Polymer 46, 12093–12102.

Roland, C.M., Twigg, J.N., Vu, Y., Mott, P.H., 2007. High strain rate mechanical behavior of polyurea. Polymer 48, 574–578.

Romano, G., Barretta, R., 2011. Covariant hypo-elasticity. European Journal of Mechanics-A/Solids 30, 1012–1023.

Sands, C.M., Chandler, H.W., 2010. Yield surfaces and flow rules for deformation of granular materials with a volume constraint. Computers and Geotechnics 37, 701–709.

Santosa, S., Wierzbicki, T., 1999. Effect of an ultralight metal filler on the bending collapse behavior of thin-walled prismatic columns. International Journal of Mechanical Sciences 41, 995–1019.

Santosa, S.P., Wierzbicki, T., Hanssen, A.G., Langseth, M., 2000. Experimental and numerical studies of foam-filled sections. International Journal of Impact Engineering 24, 509–534.

Sarva, S., Deschanel, S., Boyce, M., Chen, W., 2007. Stress–strain behavior of a polyurea and a polyurethane from low to high strain rates. Polymer 48, 2208–2213.

Schreyer, H.L., Zuo, Q.H., Maji, A.K., 1994. Anisotropic plasticity model for foams and honeycombs. ASCE Journal of Engineering Mechanics 120, 1913–1930.

Schröder-Turk, G.E., Mickel, W., Kapfer, S.C., Klatt, M.A., Schaller, F.M., Hoffmann, M.J.F., Kleppmann, N., Armstrong, P., Inayat, A., Hug, D., et al., 2011. Minkowski tensor shape analysis of cellular, granular and porous structures. Advanced Materials 23, 2535–2553.

Shahbeyk, S., Vafai, A., Estekanchi, H.E., 2004. A parametric study of the bending crash performance of empty and metal foam-filled box-beams. International Journal of Crashworthiness 9, 643–652.

Sharaf, T., Shawkat, W., Fam, A., 2010. Structural performance of sandwich wall panels with different foam core densities in one-way bending. Journal of Composite Materials 44, 2249–2263.

Song, H.W., Fan, Z.J., Yu, G., Wang, Q.C., Tobota, A., 2005. Partition energy absorption of axially crushed aluminum foam-filled hat sections. International Journal of Solids and Structures 42, 2575–2600.

Subramanian, N., Sankar, B.V., 2012. Evaluation of micromechanical methods to determine stiffness and strength properties of foams. Journal of Sandwich Structures and Materials 14, 431–447.

Xiao, H., Bruhns, O.T., Meyers, A., 1997. Logarithmic strain, logarithmic spin and logarithmic rate. Acta Mechanica 124, 89–105.

Xiao, H., Bruhns, O.T., Meyers, A., 2004. Explicit dual stress-strain and strain-stress relations of incompressible isotropic hyperelastic solids via deviatoric Hencky strain and Cauchy stress. Acta Mechanica 168, 21–33.

Xiao, H., Bruhns, O.T., Meyers, A., 2006. Elastoplasticity beyond small deformations. Acta Mechanica 182, 31–111.

Xu, J., Shim, V.P.W., Guo, Y.B., 2011. Effect of loading direction on the crushing of anisotropic polymeric foam, in: Proceedings of ITUAM Symposium: Mechanics of Solid and Liquid Foams, May 8-13, 2011, Austin, Texas.

Yue, P., Feng, J.J., Bertelo, C.A., Hu, H.H., 2007. An arbitrary Lagrangian–Eulerian method for simulating bubble growth in polymer foaming. Journal of Computational Physics 226, 2229–2249.

Zarei, H.R., Kröger, M., 2008. Bending behavior of empty and foam-filled beams: Structural optimization. International Journal of Impact Engineering 35, 521–529.

Zhang, J., Kikuchi, N., Li, V., Yee, A., Nusholtz, G., 1998. Constitutive modeling of polymeric foam material subjected to dynamic crash loading. International Journal of Impact Engineering 21, 369–386.

Zhang, T., Lee, J., 2003. A plasticity model for cellular materials with open-celled structure. International Journal of Plasticity 19, 749–770.

Zhu, H.X., Knott, J.F., Mills, N.J., 1997. Analysis of the elastic properties of open-cell foams with tetrakaidecahedral cells. Journal of the Mechanics and Physics of Solids 45, 319–343.